

BLUR IS AN ENSEMBLE: SPATIAL SMOOTHINGS TO IMPROVE ACCURACY, UNCERTAINTY, AND ROBUSTNESS

Anonymous authors

Paper under double-blind review

ABSTRACT

1 Bayesian neural networks (BNNs) have shown success in the areas of uncertainty
 2 estimation and robustness. However, a crucial challenge prohibits their use in
 3 practice. Bayesian NNs require a large number of predictions to produce reliable
 4 results, leading to a significant increase in computational cost. To alleviate this
 5 issue, we propose *spatial smoothing*, a method that ensembles neighboring feature
 6 map points of CNNs. By simply adding a few blur layers to the models, we
 7 empirically show that spatial smoothing improves accuracy, uncertainty estimation,
 8 and robustness of BNNs across a whole range of ensemble sizes. In particular,
 9 BNNs incorporating spatial smoothing achieve high predictive performance merely
 10 with a handful of ensembles. Moreover, this method also can be applied to canonical
 11 deterministic neural networks to improve the performances. A number of evidences
 12 suggest that the improvements can be attributed to the stabilized feature maps
 13 and the flattening of the loss landscape. In addition, we provide a fundamental
 14 explanation for prior works—namely, global average pooling, pre-activation, and
 15 ReLU6—by addressing them as special cases of spatial smoothing. These not
 16 only enhance accuracy, but also improve uncertainty estimation and robustness by
 17 making the loss landscape smoother in the same manner as spatial smoothing.

18 1 INTRODUCTION

19 In a real-world environment where many unexpected
 20 events occur, machine learning systems cannot be guar-
 21 anteed to always produce accurate predictions. In or-
 22 der to handle this issue, we make system decisions
 23 more reliable by considering estimated uncertainties,
 24 in addition to predictions. Uncertainty quantification is
 25 particularly crucial in building a trustworthy system in
 26 the field of safety-critical applications, including med-
 27 ical analysis and autonomous vehicle control. However,
 28 canonical deep neural networks (NNs)—or determinis-
 29 tic NNs—cannot produce reliable estimations of uncer-
 30 tainties (Guo et al., 2017), and their accuracy is often
 31 severely compromised by natural data corruptions from
 32 noise, blur, and weather changes (Engstrom et al., 2019;
 33 Azulay & Weiss, 2019).

34 Bayesian neural networks (BNNs), such as Monte Carlo
 35 (MC) dropout (Gal & Ghahramani, 2016), provide a
 36 probabilistic representation of NN weights. They com-
 37 bine a number of models selected based on weight prob-
 38 ability to make predictions of desired results. Thanks to
 39 this feature, BNNs have been widely used in the areas of uncertainty estimation (Kendall & Gal, 2017)
 40 and robustness (Ovadia et al., 2019). They are also promising in other fields like out-of-distribution
 41 detection (Malinin & Gales, 2018) and meta-learning (Yoon et al., 2018).

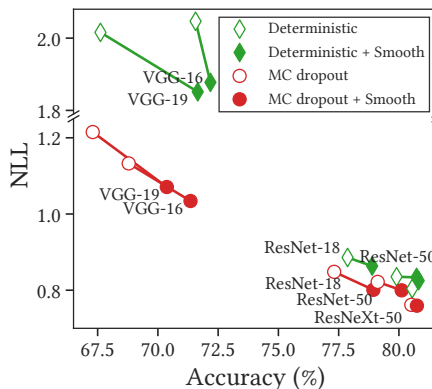


Figure 1: **Spatial smoothing improves both accuracy and uncertainty (NLL).** Smooth means spatial smoothing. Downward from left to the right (\searrow) means better accuracy and uncertainty.

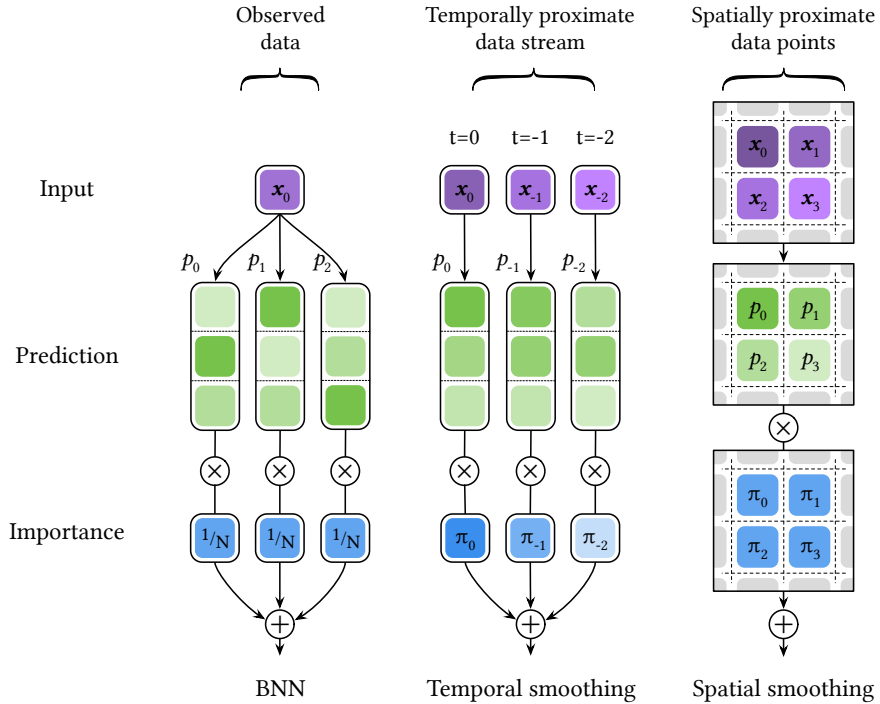


Figure 2: **Comparison of three different Bayesian neural network inferences:** canonical BNN inference, temporal smoothing (Park et al., 2021), and spatial smoothing (ours). In this figure, x_0 is observed data, p_i is predictions $p(\mathbf{y}|\mathbf{x}_0, \mathbf{w}_i)$ or $p(\mathbf{y}|\mathbf{x}_i, \mathbf{w}_i)$, π_i is importances $\pi(\mathbf{x}_i|\mathbf{x}_0)$, and N is ensemble size.

42 Nevertheless, there remains a significant challenge that prohibits their use in practice. BNNs require
 43 an ensemble size of up to fifty to achieve high predictive performance, which results in a fiftyfold
 44 increase in computational cost (Kendall & Gal, 2017; Loquercio et al., 2020). Therefore, if BNNs
 45 can achieve high predictive performance merely with a handful of ensembles, they could be applied
 46 to a much wider range of areas.

47 1.1 PRELIMINARY

48 We would first like to discuss BNN inference in detail, then move on to Vector-Quantized BNN
 49 (VQ-BNN) inference (Park et al., 2021), an efficient approximated BNN inference.

BNN inference. Suppose we have access to posterior probability of NN weight $p(\mathbf{w}|\mathcal{D})$ for training dataset \mathcal{D} . The predictive result of BNN is given by the following predictive distribution:

$$p(\mathbf{y}|\mathbf{x}_0, \mathcal{D}) = \int p(\mathbf{y}|\mathbf{x}_0, \mathbf{w}) p(\mathbf{w}|\mathcal{D}) d\mathbf{w} \tag{1}$$

where \mathbf{x}_0 is observed input data vector, \mathbf{y} is output vector, and $p(\mathbf{y}|\mathbf{x}, \mathbf{w})$ is the probabilistic prediction parameterized by the result of NN for an input \mathbf{x} and weight \mathbf{w} . In most cases, the integral cannot be solved analytically. Thus, we use the MC estimator to approximate it as follows:

$$p(\mathbf{y}|\mathbf{x}_0, \mathcal{D}) \simeq \sum_{i=0}^{N-1} \frac{1}{N} p(\mathbf{y}|\mathbf{x}_0, \mathbf{w}_i) \tag{2}$$

50 where $\mathbf{w}_i \sim p(\mathbf{w}|\mathcal{D})$ and N is the number of the samples. The equation indicates that *BNN inference*
 51 *is ensemble average of NN predictions for one observed data point* as shown on the left of Fig. 2.
 52 Using N neural networks in the ensemble would requires N times more computational complexity
 53 than one NN execution.

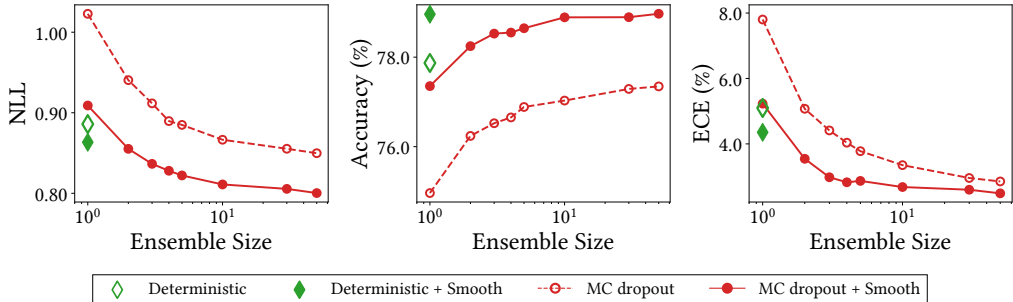


Figure 3: **Spatial smoothing improves both accuracy and uncertainty across a whole range of ensemble sizes.** We report the predictive performance of ResNet-18 on CIFAR-100.

Data-complemented BNN inference. To reduce the computational cost of BNN inference, *VQ-BNN* (Park et al., 2021) executes NN for an observed data only once and complements the result with previously calculated predictions for other data. If we have access to previous predictions, the computational performance of VQ-BNN becomes comparable to that of one NN execution. To be specific, VQ-BNN inference is:

$$p(\mathbf{y}|\mathbf{x}_0, \mathcal{D}) \simeq \sum_{i=0}^{N-1} \pi(\mathbf{x}_i|\mathbf{x}_0) p(\mathbf{y}|\mathbf{x}_i, \mathbf{w}_i) \quad (3)$$

54 where $\pi(\mathbf{x}_i|\mathbf{x}_0)$ is the importance of data \mathbf{x}_i with respect to the observed data \mathbf{x}_0 , and it is defined as a
 55 similarity between \mathbf{x}_i and \mathbf{x}_0 . $p(\mathbf{y}|\mathbf{x}_0, \mathbf{w}_0)$ is the newly calculated prediction, and $\{p(\mathbf{y}|\mathbf{x}_1, \mathbf{w}_1), \dots\}$
 56 are previously calculated predictions. To accurately infer the results, *the previous predictions should*
 57 *consist of predictions for “data similar to the observed data”.*

58 Thanks to the temporal consistency of real-world data streams, aggregating predictions for similar
 59 data in data streams is straightforward. Since temporally proximate data sequences tend to be similar,
 60 we can memorize recent predictions and calculates their average using exponentially decreasing
 61 importance. In other words, *VQ-BNN inference for data streams is simply temporal smoothing of*
 62 *recent predictions* as shown in the middle of Fig. 2.

63 VQ-BNN has two limitations, although it may be a promising approach to obtain reliable results
 64 in an efficient way. First, it was only applicable to data streams such as video sequences. Applying
 65 VQ-BNN to images is challenging because it is impossible to memorize all similar images in advance.
 66 Second, Park et al. (2021) used VQ-BNN only in the testing phase, not in the training phase. We find
 67 that ensembling predictions for similar data helps in NN training by smoothing the loss landscape.

68 1.2 MAIN CONTRIBUTION

69 **1** Spatially neighboring points in visual imagery tend to be similar, as do feature maps of convolu-
 70 tional neural networks (CNNs). By exploiting this spatial consistency, *we propose spatial smoothing*
 71 *as a method of ensembling nearby feature maps* to improve the efficiency of ensemble size in BNN
 72 inference. The right side of Fig. 2 visualizes spatial smoothing aggregating neighboring feature maps.

73 **2** We empirically demonstrate that spatial smoothing improves the efficiency in vision tasks, such
 74 as image classification on CIFAR (Krizhevsky et al., 2009) and ImageNet (Russakovsky et al., 2015),
 75 without any additional training parameters. Figure 3 shows that negative log-likelihood (NLL) of
 76 “MC dropout + spatial smoothing” with an ensemble size of two is comparable to that of vanilla MC
 77 dropout with an ensemble size of fifty. We also demonstrate that spatial smoothing improves accuracy,
 78 uncertainty, and robustness all at the same time. Figure 1 shows that spatial smoothing improves both
 79 the accuracy and uncertainty of various deterministic and Bayesian NNs with an ensemble size of
 80 fifty on CIFAR-100.

81 **3** Global average pooling (GAP) (Lin et al., 2014; Zhou et al., 2016), pre-activation (He et al.,
 82 2016b), and ReLU6 (Krizhevsky & Hinton, 2010; Sandler et al., 2018) have been widely used in vision
 83 tasks. However, their motives are largely justified by the experiments. We provide an explanation for
 84 these methods by addressing them as special cases of spatial smoothing. Experiments support the
 85 claim by showing that the methods improve not only accuracy but also uncertainty and robustness.

86 2 PROBABILISTIC SPATIAL SMOOTHING

87 To improve the computational perfor-
 88 mance of BNN inference, VQ-BNN
 89 (Park et al., 2021) executes NN pre-
 90 diction only once and complements
 91 the result with previously calculated
 92 predictions. The key to the success
 93 of this approach largely depends on
 94 the collection of previous predictions
 95 for proximate data. Gathering tempo-
 96 rally proximate data and their predic-
 97 tions from data streams is easy be-
 98 cause recent data and predictions can
 99 be aggregated using temporal consis-
 100 tency. On the other hand, gathering
 101 time-independent proximate data, e.g. images, is more difficult because they lack such consistency.

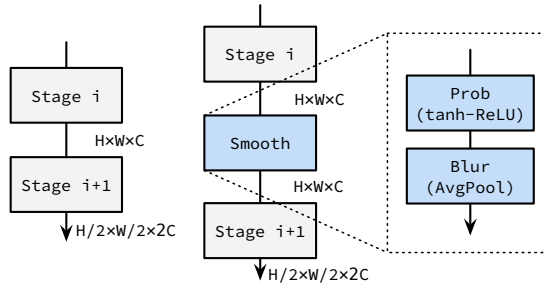


Figure 4: Stages of CNNs such as ResNet (left) and the stages incorporating spatial smoothing layer (right).

102 2.1 MODULE ARCHITECTURE FOR ENSEMBLING NEIGHBORING FEATURE MAP POINTS

103 So instead of temporal consistency, we use spatial consistency—where neighboring pixels of images
 104 are similar—for real-world images. Under this hypothesis, we take the feature maps as predictions
 105 and aggregate neighboring feature maps.

Most CNN architectures, including ResNet, consist of multiple stages that begin with increasing the number of channels while reducing the spatial dimension of the input volume. We decompose an entire BNN inference into several steps by rewriting each stage in a recurrence relation as follows:

$$p(\mathbf{z}_{i+1}|\mathbf{z}_i, \mathcal{D}) = \int p(\mathbf{z}_{i+1}|\mathbf{z}_i, \mathbf{w}_i) p(\mathbf{w}_i|\mathcal{D}) d\mathbf{w}_i \quad (4)$$

106 where \mathbf{z}_i is input volume of the i -th stage, and the first and the last volume are input data and
 107 output. \mathbf{w}_i and $p(\mathbf{w}_i|\mathcal{D})$ are NN weight in the i -th stage and its probability. $p(\mathbf{z}_{i+1}|\mathbf{z}_i, \mathbf{w}_i)$ is output
 108 probability of \mathbf{z}_{i+1} with respect to the input volume \mathbf{z}_i . To derive the probability from the output
 109 feature map, we transform each point of the feature map into a Bernoulli distribution. To do so, a
 110 composition of \tanh and ReLU, a function from value of range $[-\infty, \infty]$ into probability, is added
 111 after each stage. Put shortly, we use neural networks for *point-wise binary feature classification*.

112 Since Eq. (4) is a kind of BNN inference, it can be approximated using Eq. (3). In other words, each
 113 stage predicts feature map points only once and complements predictions with similar feature maps.
 114 Under spatial consistency, it averages probabilities of spatially neighboring feature map points, which
 115 is well known as *blur* operation in image processing. For the sake of implementation simplicity,
 116 average pooling with a kernel size of 2 and a stride of 1 is used as a box blur. This operation ensembles
 117 four neighboring probabilities with the same importances.

In summary, as shown in Fig. 4, we propose the following *probabilistic spatial smoothing* layer:

$$\text{Smooth}(\mathbf{z}) = \text{Blur} \circ \text{Prob}(\mathbf{z}) \quad (5)$$

118 where $\text{Prob}(\cdot)$ is a point-wise function from a feature map to probability, and $\text{Blur}(\cdot)$ is importance-
 119 weighted average for ensembling spatially neighboring probabilities from feature maps. Smooth layer
 120 is added after each stage. Prob and Blur are further elaborated below.

Prob: Feature map to probability. Prob is a function that transforms a real-valued feature map into probability. We use \tanh -ReLU composition for this purpose. However, \tanh is commonly known to suffer from the vanishing gradient problem. To alleviate this issue, we propose the following temperature-scaled \tanh :

$$\tanh_\tau(\mathbf{z}) = \tau \tanh(\mathbf{z}/\tau) \quad (6)$$

121 where τ is a hyperparameter called temperature. τ is 1 in conventional \tanh and ∞ in identity
 122 function. \tanh_τ imposes an upper bound on a value, but does not limit the upper bound to 1.

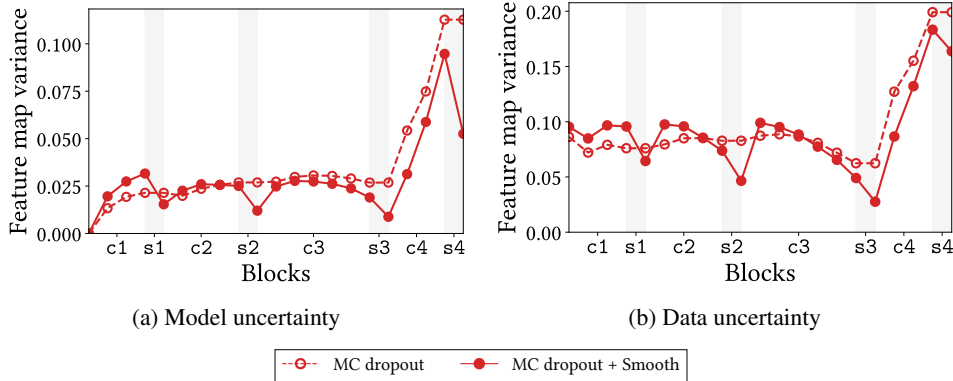


Figure 5: **Spatial smoothing layers reduce feature map variances**, suggesting that they ensemble feature map points. We provide standard deviation of feature maps by block depth with ResNet-50 on CIFAR-100. $c1$ to $c4$ and $s1$ to $s4$ each stand for stages and spatial smoothing layers, respectively. Model uncertainty is represented by the average standard deviation of several feature maps obtained from multiple NN executions. Data uncertainty is represented by the standard deviation of feature map points obtained from one NN execution.

An unnormalized probability, ranging from 0 to τ , is allowed as the output of Prob. Then, thanks to the linearity of integration, we obtain an unnormalized predictive distribution accordingly. Taking this into account, we propose the following Prob:

$$\text{Prob}(z) = \text{ReLU} \circ \tanh_{\tau}(z) \quad (7)$$

123 where $\tau > 1$. We empirically determine τ to minimize NLL, a metric that measures both accuracy
 124 and uncertainty. See Fig. B.3 for more detailed ablation studies. In addition, we expect upper-bounded
 125 functions, e.g., $\text{ReLU6}(z) = \text{ReLU} \circ \min(z, 6)$ and feature map scaling z/τ with $\tau > 1$ which
 126 is BatchNorm, to be able to replace \tanh_{τ} in Prob; and as expected, these alternatives improve
 127 uncertainty estimation in addition to accuracy. See Appendix C.2 and Appendix C.3 for detailed
 128 discussions on activation ($\text{ReLU} \circ \text{BatchNorm}$) and ReLU6 as Prob.

Blur: Averaging neighboring probabilities. Blur averages the probabilities from feature maps. We primarily use the average pool with a kernel size of 2 and a stride of 1 as the implementation of Blur for the sake of simplicity. Nevertheless, we could generalize Blur by using the following depth-wise convolution, which acts on each input channel separately, with non-trainable kernel

$$\mathbf{K} = \frac{1}{\|\mathbf{k}\|_1^2} \mathbf{k} \otimes \mathbf{k}^{\top} \quad (8)$$

129 where \mathbf{k} is a 1D matrix, e.g., $\mathbf{k} \in \{(1), (1, 1), (1, 2, 1), (1, 4, 6, 4, 1)\}$. Different \mathbf{k} s derive different
 130 importances for neighboring feature maps. We empirically show that most Blurs improve the
 131 predictive performance and that optimal \mathbf{K} varies by model. For more ablation studies, see Table B.2.

132 2.2 HOW DOES SPATIAL SMOOTHING HELP OPTIMIZATION?

133 We present theoretical and empirical aspects to show that *spatial smoothing ensembles feature maps*.

134 **Feature map variance.** BNNs have two types of uncertainties: One is model uncertainty and the
 135 other is data uncertainty (Park et al., 2021). These randomnesses increase the variance of the feature
 136 maps. To demonstrate that spatial smoothing is an ensemble, we use the following proposition:

137 **Proposition 1.** *Ensembles reduce the variance of predictions.*

138 We omit the proof since it is straightforward. In our context, predictions are output feature maps of a
 139 stage. We investigate model and data uncertainties of the predictions along NN layers to show that
 140 spatial smoothing reduces the randomnesses and ensembles feature maps. Figure 5 shows the model
 141 uncertainty and data uncertainty of Bayesian ResNet including MC dropout layers. In this figure, the

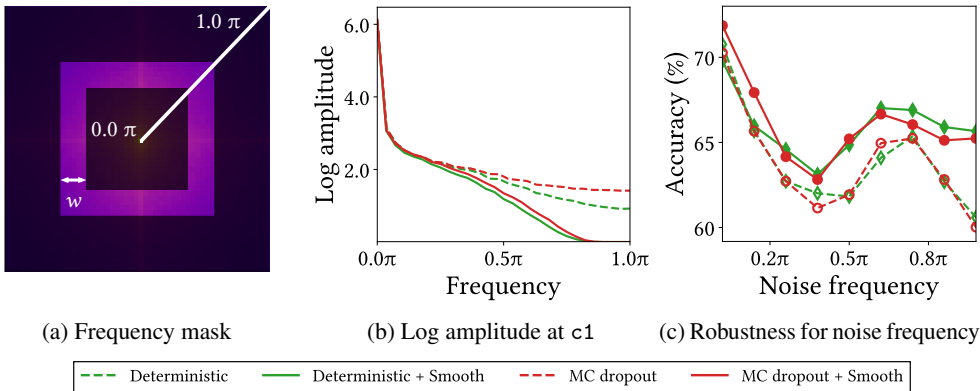


Figure 6: **MC dropout adds high-frequency noises, and spatial smoothing filters high-frequency signals.** In these experiments, we use ResNet-50 for ImageNet. *Left:* Frequency mask \mathbf{M}_f with $w = 0.1\pi$. *Middle:* Diagonal components of Fourier transformed feature maps at the end of the stage 1. *Right:* The accuracy against frequency-based random noise. ResNets are vulnerable to high-frequency noises. Spatial smoothing improves the robustness against high-frequency noises.

142 uncertainty of MC dropout’s feature map only accumulates, and almost monotonically increases in
 143 every NN layer. In contrast, the uncertainty of “MC dropout + spatial smoothing”’s feature map is
 144 significantly decreases at the end of stages, suggesting that the smoothing layers ensemble the feature
 145 map. In other words, they make the feature map more accurate and stabilized input volumes for the
 146 next stages. In addition, consistently, the spatial smoothing layer close to the last layer significantly
 147 improves performance because it reduces the uncertainty of predictions largely. See Fig. B.5 for more
 148 detailed results. Deterministic NNs do not have model uncertainty but data uncertainty. Therefore,
 149 spatial smoothing improves the performance of deterministic NNs as well as Bayesian NNs.

150 **Fourier analysis.** We also analyze spatial smoothing through the lens of Fourier transform:

151 **Proposition 2.** *Ensembles filter high-frequency signals.*

152 The proof is provided in Eqs. (16) to (17). Figure 6b shows the 2D Fourier transformed output
 153 feature map at the end of the stage 1. This figure reveals that MC dropout almost does not affect
 154 low-frequency ($< 0.3\pi$) ranges, and it adds high-frequency ($\geq 0.3\pi$) noises. Since spatial smoothing
 155 is a low-pass filter, it effectively filters high-frequency signals, including the noises caused by MC
 156 dropout.

157 We also find that CNNs are particularly vulnerable to high-frequency noises. To demonstrate this
 158 claim, following Shao et al. (2021), we measure accuracy with respect to data with frequency-based
 159 random noise $\mathbf{x}_{\text{noise}} = \mathbf{x}_0 + \mathcal{F}^{-1}(\mathcal{F}(\delta) \odot \mathbf{M}_f)$, where \mathbf{x}_0 is clean data, $\mathcal{F}(\cdot)$ and $\mathcal{F}^{-1}(\cdot)$ are Fourier
 160 transform and inverse Fourier transform, δ is random noise, and \mathbf{M}_f is frequency mask as shown
 161 in Fig. 6a. Figure 6c exhibits the results. In sum, high-frequency noises, including those caused by
 162 MC dropout, significantly impair accuracy. Spatial smoothing improves the robustness by effectively
 163 removing high-frequency noises.

164 **Loss landscape.** Lastly, we show that the randomness hinders NN training as follows:

165 **Proposition 3.** *Randomness of predictions sharpens the loss landscape, and ensembles flatten it.*

166 The proof is provided in Eqs. (18) to (25). Since a sharp loss function disturbs NN optimization
 167 (Keskar et al., 2017; Santurkar et al., 2018; Foret et al., 2020), reducing the uncertainty helps NN
 168 learn strong representations. For example, training phase NN ensemble averages out the randomness,
 169 and it flattens the loss function. In consequence, an ensemble of BNN outputs in training phase
 170 significantly improves the predictive performance. See Fig. D.4 for numerical results. However, we
 171 do not use training phase ensemble because it significantly increases the training time. Instead, we
 172 use spatial smoothing as a method that ensembles feature maps without sacrificing training time.

173 We visualizes the loss landscapes (Li et al., 2018), the contours of NLL on training dataset. Figure 8b
 174 shows that the loss landscapes of MC dropout fluctuate and have irregular surfaces due to the

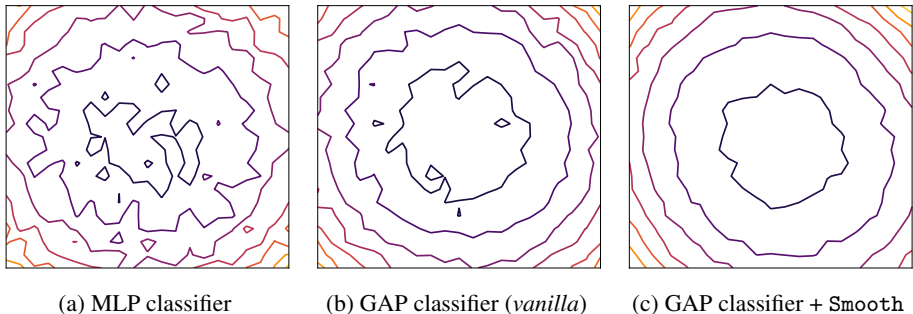


Figure 8: **Both GAP and spatial smoothing smoothen the loss landscapes.** To demonstrate this, we present the loss landscape visualizations of ResNet-18 models with MC dropout on CIFAR-100.

175 randomness. As Li et al. (2018); Foret et al. (2020) pointed out,
 176 this may lead to poor generalization and predictive performance.
 177 Spatial smoothing reduces randomness as discussed above, and
 178 *spatial smoothing aids in optimization by stabilizing and flattening*
 179 *the loss landscape of BNN* as shown in Fig. 8c.

180 Furthermore, we use Hessian to quantitatively represent the sharp-
 181 ness of the loss landscapes. Figure 7 shows the Hessian max eigen-
 182 value spectra of the models in Fig. 8 with a batch size of 128, which
 183 reveals that spatial smoothing reduces the magnitude of Hessian
 184 eigenvalues and suppresses outliers. Since large Hessian eigenval-
 185 ues disturb NN training (Ghorbani et al., 2019), we come to the
 186 same conclusion that spatial smoothing helps NN optimization. See
 187 Appendix C.1 for a more detailed description of the configurations
 188 of the Hessian max eigenvalue spectra. In addition, from these
 189 observations, we propose the conjecture that the flatter the loss
 190 landscape, the better the uncertainty estimation, and vice versa.

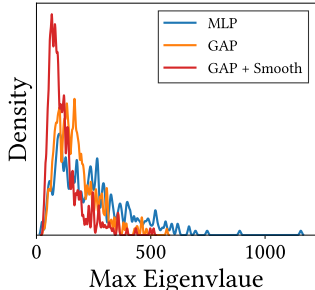


Figure 7: **Both GAP and spatial smoothing suppress large Hessian eigenvalue outliers,** i.e., they flatten the loss landscapes. Compare with Fig. 8.

191 2.3 REVISITING GLOBAL AVERAGE POOLING

192 The success of GAP classifier in image classification is indisputable. The initial motivation and the most widely
 193 accepted explanation for this success is that GAP prevents
 194 overfitting by using far fewer parameters than multi-layer
 195 perceptron (MLP) (Lin et al., 2014). However, we discover
 196 that the explanation is poorly supported. We compares
 197 GAP with other classifiers including MLP. Contrary to
 198 popular belief, Table 1 suggests that *MLP does not overfit*
 199 *the training dataset*. MLP underfits or gives comparable
 200 performance to GAP on the training dataset. On the test
 201 dataset, GAP provides better results compared with MLP. See Table C.1 for more detailed results.

Table 1: **MLP does not overfit the training dataset.** We report training NLL (NLL_{train}) and testing NLL (NLL_{test}) of ResNet-50 on CIFAR-100.

CLASSIFIER	NLL_{train}	NLL_{test}
GAP	0.0061	0.822
MLP	0.0071	1.029

203 Our argument is that GAP is an extreme case of spatial smoothing. In other words, GAP is successful
 204 because it ensembles feature maps and smoothen the loss landscape to help optimization. To support
 205 this claim, we visualizes the loss landscape of MLP as shown in Fig. 8a. It is chaotic compared to
 206 that of GAP as shown in Fig. 8b. Hessian shows the consistent results as demonstrated by Fig. 7.

207 3 EXPERIMENTS

208 This section presents two experiments. The first experiment is image classification through which
 209 we show that spatial smoothing not only improves the ensemble efficiency, but also the accuracy,
 210 uncertainty, and robustness of both deterministic NN and MC dropout. The second experiment is
 211 semantic segmentation on data streams through which we show that spatial smoothing and temporal
 212 smoothing (Park et al., 2021) are complementary. See Appendix A for more detailed configurations.

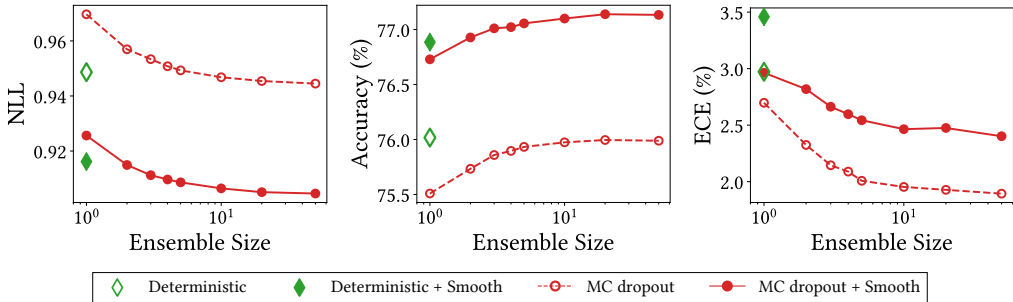


Figure 9: **Spatial smoothing also improves predictive performance on large datasets.** We report predictive performance of ResNet-50 on ImageNet.

213 Three metrics are measured in these experiments: NLL (\downarrow^1), accuracy (\uparrow), and expected calibration
 214 error (ECE, \downarrow) (Guo et al., 2017). NLL represents both accuracy and uncertainty, and is the most
 215 widely used as a proper scoring rule. ECE measures discrepancy between accuracy and confidence.

216 3.1 IMAGE CLASSIFICATION

217 This section mainly discuss ResNet (He et al., 2016a). Table E.1 also discuss other settings that
 218 show the same trend: e.g., VGG (Simonyan & Zisserman, 2015), ResNeXt (Xie et al., 2017),
 219 and pre-activation models (He et al., 2016a). Spatial smoothing also improves deep ensemble
 220 (Lakshminarayanan et al., 2017), another non-Bayesian probabilistic NN method. See Fig. E.1.

221 **Performance.** Fig. 3 and Fig. 9 show the predictive performances of ResNet-18 on CIFAR-100
 222 and ResNet-50 on ImageNet, respectively. The results indicate that *spatial smoothing improves both*
 223 *accuracy and uncertainty* in many respects. Let us be more specific. First, spatial smoothing improves
 224 the efficiency of ensemble size. In these examples, the NLL of “MC dropout + spatial smoothing”
 225 with an ensemble size of 2 is comparable to or even better than that of MC dropout with an ensemble
 226 size of 50. In other words, “MC dropout + spatial smoothing” is $25\times$ faster than MC dropout with
 227 a similar predictive performance. Second, the predictive performance of “MC dropout + spatial
 228 smoothing” is better than that of MC dropout, at an ensemble size of 50. Third, spatial smoothing
 229 improves the predictive performance of deterministic NN, as well as MC dropout.

230 **Robustness.** To evaluate robustness against data corruption, we
 231 measure predictive performance of ResNet-18 on CIFAR-100-
 232 C (Hendrycks & Dietterich, 2019). This dataset consists of data
 233 corrupted by 15 different types, each with 5 levels of intensity
 234 each. We use mean corruption NLL (mCNLL, \downarrow), the averages
 235 of NLL over intensities and corruption types, to summarize the
 236 performance of corrupted data in a single value. See Eq. (32) for
 237 a more rigorous definition. Figure 10 shows that spatial smoothing
 238 not only improves the efficiency but also corruption robustness
 239 across a whole range of ensemble size. See Fig. E.3 for more
 240 details. Spatial smoothing also improves adversarial robustness
 241 and perturbation consistency (\uparrow) (Hendrycks & Dietterich, 2019;
 242 Zhang, 2019a), shift-transformation invariance. See Table E.2,
 243 Table E.3, and Fig. E.4 for more details.

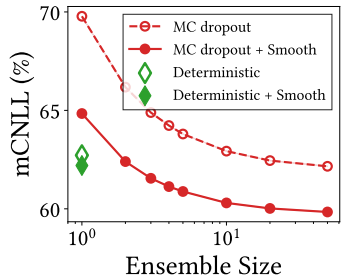


Figure 10: **Spatial smoothing improves the robustness.** See Fig. E.3 for more details.

244 3.2 SEMANTIC SEGMENTATION

245 Table 2 summarizes the result of semantic segmentation on CamVid dataset (Brostow et al., 2008)
 246 that consists of real-world 360×480 pixels videos. The table shows that spatial smoothing improves
 247 predictive performance, which is consistent with the image classification experiment. Moreover, the
 248 result reveals that *spatial smoothing and temporal smoothing* (Park et al., 2021) are complementary.
 249 See Table E.4 for more results.

¹We use arrows to indicate which direction is better.

Table 2: **Spatial smoothing and temporal smoothing are complementary.** We provide predictive performance of MC dropout in semantic segmentation. SPAT and TEMP each stand for spatial smoothing and temporal smoothing. ACC and CONS stand for accuracy and consistency. The numbers in brackets denote the performance improvements over the baseline.

SPAT	TEMP	NLL	ACC (%)	ECE (%)	CONS (%)
.	.	0.298 (-0.000)	92.5 (+0.0)	4.20 (-0.00)	95.4 (+0.0)
✓	.	0.284 (-0.014)	92.6 (+0.1)	3.96 (-0.24)	95.6 (+0.2)
.	✓	0.273 (-0.025)	92.6 (+0.1)	3.23 (-0.97)	96.4 (+1.0)
✓	✓	0.260 (-0.038)	92.6 (+0.1)	2.71 (-1.49)	96.5 (+1.1)

250 4 RELATED WORK

251 Spatial smoothing can be compared with prior works in the following areas.

252 **Anti-aliased CNNs.** Local means (Zhang, 2019a; Zou et al., 2020; Vasconcelos et al., 2020; Sinha
 253 et al., 2020) were introduced for the shift-invariance of deterministic CNNs in image classification.
 254 They were motivated to prevent the aliasing effect of subsampling. Although the local filtering can
 255 result in a loss of information, Zhang (2019a) experimentally observed an increase in accuracy that
 256 was beyond expectation. We provide a fundamental explanation for this phenomenon: *Local means*
 257 *are a spatial ensemble*. An ensemble not only improves accuracy, but also uncertainty and robustness
 258 of deterministic and Bayesian NNs. In Fig. F.1, we also show that *the predictive performance*
 259 *improvement is not due to anti-aliasing of local mean*. See Appendix F for more discussion on local
 260 means. For a discussion on non-local means (Wang et al., 2018) and self-attention (Dosovitskiy et al.,
 261 2021), see Section 5.

262 **Sampling-free BNNs.** Sampling-free BNNs (Hernández-Lobato & Adams, 2015; Wang et al.,
 263 2016; Wu et al., 2019) predict results based on a single or couple of NN executions. To this end, it is
 264 assumed that posterior and feature maps follow Gaussian distributions. However, the discrepancy
 265 between reality and assumption accumulates in every NN layer. Consequently, to the best of our
 266 knowledge, most of the sampling-free BNNs could only be applied to shallow models, such as LeNet,
 267 and were tested on small datasets. Postels et al. (2019) applied sampling-free BNNs to SegNet;
 268 nonetheless, Park et al. (2021) argued that they do not predict well-calibrated results.

269 **Efficient deep ensembles.** Deep ensemble (Lakshminarayanan et al., 2017; Fort et al., 2019) is
 270 another probabilistic NN approach for predicting reliable results. BatchEnsemble (Wen et al., 2020;
 271 Dusenberry et al., 2020) ensembles over a low-rank subspace to make deep ensemble more efficient.
 272 Depth uncertainty network (Antoran et al., 2020) aggregates feature maps from different depths of
 273 a single NN to predict results efficiently. Despite being robust against data corruption, it provides
 274 weaker predictive performance compared to deterministic NN and MC dropout.

275 5 DISCUSSION

276 We propose spatial smoothing, a simple yet efficient module to improve BNN. Three different per-
 277 spectives, namely, feature map variance, Fourier analysis, and loss landscape, suggest that spatial
 278 smoothing ensembles feature maps. The limitation of spatial smoothing is that designing its compo-
 279 nents requires inductive bias. In other words, the optimal shape of the blur kernel is model-dependent.
 280 We believe this problem can be solved by introducing self-attention (Vaswani et al., 2017). Self-
 281 attentions for computer vision (Dosovitskiy et al., 2021; Touvron et al., 2021; Carion et al., 2020)
 282 can be deemed as trainable importance-weighted ensembles of feature maps. The observation that
 283 Transformers are more robust than expected (Bhojanapalli et al., 2021; Shao et al., 2021) supports this
 284 claim. Therefore, using self-attentions to generalize spatial smoothing would be a promising future
 285 work because it not only expands our work, but also helps deepen our understanding of self-attention.

286 REPRODUCIBILITY STATEMENT

287 To ensure reproducibility, we provide comprehensive resources, such as code and experimental details.
 288 The codebase will be released as open source under the Apache License 2.0. See the supplemental
 289 material for the code. [Appendix A](#) provides the specifications of all models used in this work. Detailed
 290 experimental setup including hyperparameters and ablation study are also available in [Appendix A](#)
 291 and [Appendix B](#). De-facto image datasets are used for all experiments as described in [Appendix A](#).

292 REFERENCES

- 293 Javier Antoran, James Allingham, and José Miguel Hernández-Lobato. Depth uncertainty in neural
 294 networks. *Advances in Neural Information Processing Systems*, 2020.
- 295 Aharon Azulay and Yair Weiss. Why do deep convolutional networks generalize so poorly to small
 296 image transformations? *Journal of Machine Learning Research*, 2019.
- 297 Srinadh Bhojanapalli, Ayan Chakrabarti, Daniel Glasner, Daliang Li, Thomas Unterthiner, and
 298 Andreas Veit. Understanding robustness of transformers for image classification. In *Proceedings*
 299 *of the IEEE/CVF International Conference on Computer Vision*, 2021.
- 300 Gabriel J Brostow, Jamie Shotton, Julien Fauqueur, and Roberto Cipolla. Segmentation and recog-
 301 nition using structure from motion point clouds. In *European Conference on Computer Vision*.
 302 Springer, 2008.
- 303 Nicolas Carion, Francisco Massa, Gabriel Synnaeve, Nicolas Usunier, Alexander Kirillov, and Sergey
 304 Zagoruyko. End-to-end object detection with transformers. In *European Conference on Computer*
 305 *Vision*. Springer, 2020.
- 306 Alexey Dosovitskiy, Lucas Beyer, Alexander Kolesnikov, Dirk Weissenborn, Xiaohua Zhai, Thomas
 307 Unterthiner, Mostafa Dehghani, Matthias Minderer, Georg Heigold, Sylvain Gelly, et al. An image
 308 is worth 16x16 words: Transformers for image recognition at scale. In *International Conference*
 309 *on Learning Representations*, 2021.
- 310 Michael Dusenberry, Ghassen Jerfel, Yeming Wen, Yian Ma, Jasper Snoek, Katherine Heller, Balaji
 311 Lakshminarayanan, and Dustin Tran. Efficient and scalable bayesian neural nets with rank-1
 312 factors. In *International Conference on Machine Learning*. PMLR, 2020.
- 313 Logan Engstrom, Brandon Tran, Dimitris Tsipras, Ludwig Schmidt, and Aleksander Madry. Exploring
 314 the landscape of spatial robustness. In *International Conference on Machine Learning*. PMLR,
 315 2019.
- 316 Pierre Foret, Ariel Kleiner, Hossein Mobahi, and Behnam Neyshabur. Sharpness-aware minimization
 317 for efficiently improving generalization. In *International Conference on Learning Representations*,
 318 2020.
- 319 Stanislav Fort, Huiyi Hu, and Balaji Lakshminarayanan. Deep ensembles: A loss landscape perspec-
 320 tive. *arXiv preprint arXiv:1912.02757*, 2019.
- 321 Jonathan Frankle, David J Schwab, and Ari S Morcos. Training batchnorm and only batchnorm:
 322 On the expressive power of random features in cnns. In *International Conference on Learning*
 323 *Representations*, 2021.
- 324 Yarin Gal and Zoubin Ghahramani. Dropout as a bayesian approximation: Representing model
 325 uncertainty in deep learning. In *International Conference on Machine Learning*. PMLR, 2016.
- 326 Robert Geirhos, Patricia Rubisch, Claudio Michaelis, Matthias Bethge, Felix A Wichmann, and
 327 Wieland Brendel. Imagenet-trained cnns are biased towards texture; increasing shape bias improves
 328 accuracy and robustness. In *International Conference on Learning Representations*, 2019.
- 329 Behrooz Ghorbani, Shankar Krishnan, and Ying Xiao. An investigation into neural net optimization
 330 via hessian eigenvalue density. In *International Conference on Machine Learning*. PMLR, 2019.

- 331 Ian J Goodfellow, Jonathon Shlens, and Christian Szegedy. Explaining and harnessing adversarial
332 examples. *International Conference on Learning Representations*, 2015.
- 333 Priya Goyal, Piotr Dollár, Ross Girshick, Pieter Noordhuis, Lukasz Wesolowski, Aapo Kyrola,
334 Andrew Tulloch, Yangqing Jia, and Kaiming He. Accurate, large minibatch sgd: Training imagenet
335 in 1 hour. *arXiv preprint arXiv:1706.02677*, 2017.
- 336 Chuan Guo, Geoff Pleiss, Yu Sun, and Kilian Q Weinberger. On calibration of modern neural
337 networks. In *International Conference on Machine Learning*. PMLR, 2017.
- 338 Kaiming He, Xiangyu Zhang, Shaoqing Ren, and Jian Sun. Deep residual learning for image
339 recognition. In *Proceedings of the IEEE Conference on Computer Vision and Pattern Recognition*,
340 2016a.
- 341 Kaiming He, Xiangyu Zhang, Shaoqing Ren, and Jian Sun. Identity mappings in deep residual
342 networks. In *European Conference on Computer Vision*. Springer, 2016b.
- 343 Dan Hendrycks and Thomas Dietterich. Benchmarking neural network robustness to common
344 corruptions and perturbations. In *International Conference on Learning Representations*, 2019.
- 345 José Miguel Hernández-Lobato and Ryan Adams. Probabilistic backpropagation for scalable learning
346 of bayesian neural networks. In *International Conference on Machine Learning*. PMLR, 2015.
- 347 Elad Hoffer, Tal Ben-Nun, Itay Hubara, Niv Giladi, Torsten Hoefler, and Daniel Soudry. Augment
348 your batch: Improving generalization through instance repetition. In *Proceedings of the IEEE/CVF*
349 *Conference on Computer Vision and Pattern Recognition*, 2020.
- 350 A Kendall, V Badrinarayanan, and R Cipolla. Bayesian segnet: Model uncertainty in deep convolu-
351 tional encoder-decoder architectures for scene understanding. In *BMVC*, 2017.
- 352 Alex Kendall and Yarin Gal. What uncertainties do we need in bayesian deep learning for computer
353 vision? *Advances in Neural Information Processing Systems*, 2017.
- 354 Nitish Shirish Keskar, Dheevatsa Mudigere, Jorge Nocedal, Mikhail Smelyanskiy, and Ping Tak Peter
355 Tang. On large-batch training for deep learning: Generalization gap and sharp minima. In
356 *International Conference on Learning Representations*, 2017.
- 357 Alex Krizhevsky and Geoff Hinton. Convolutional deep belief networks on cifar-10. *Unpublished*
358 *manuscript*, 2010.
- 359 Alex Krizhevsky, Geoffrey Hinton, et al. Learning multiple layers of features from tiny images. 2009.
- 360 Balaji Lakshminarayanan, Alexander Pritzel, and Charles Blundell. Simple and scalable predictive
361 uncertainty estimation using deep ensembles. In *Advances in Neural Information Processing*
362 *Systems*, 2017.
- 363 Hao Li, Zheng Xu, Gavin Taylor, Christoph Studer, and Tom Goldstein. Visualizing the loss landscape
364 of neural nets. In *Advances in Neural Information Processing Systems*, 2018.
- 365 Min Lin, Qiang Chen, and Shuicheng Yan. Network in network. In *International Conference on*
366 *Learning Representations*, 2014.
- 367 Antonio Loquercio, Mattia Segu, and Davide Scaramuzza. A general framework for uncertainty
368 estimation in deep learning. *IEEE Robotics and Automation Letters*, 2020.
- 369 Aleksander Madry, Aleksandar Makelov, Ludwig Schmidt, Dimitris Tsipras, and Adrian Vladu.
370 Towards deep learning models resistant to adversarial attacks. In *International Conference on*
371 *Learning Representations*, 2018.
- 372 A Malinin and M Gales. Predictive uncertainty estimation via prior networks. In *Advances in Neural*
373 *Information Processing Systems*. Curran Associates, Inc., 2018.
- 374 Yaniv Ovadia, Emily Fertig, Jie Ren, Zachary Nado, David Sculley, Sebastian Nowozin, Joshua
375 Dillon, Balaji Lakshminarayanan, and Jasper Snoek. Can you trust your model’s uncertainty?
376 evaluating predictive uncertainty under dataset shift. In *Advances in Neural Information Processing*
377 *Systems*, 2019.

- 378 Namuk Park, Taekyu Lee, and Songkuk Kim. Vector quantized bayesian neural network inference
379 for data streams. In *AAAI Conference on Artificial Intelligence*, 2021.
- 380 Adam Paszke, Sam Gross, Francisco Massa, Adam Lerer, James Bradbury, Gregory Chanan, Trevor
381 Killeen, Zeming Lin, Natalia Gimelshein, Luca Antiga, et al. Pytorch: An imperative style,
382 high-performance deep learning library. *Advances in Neural Information Processing Systems*,
383 2019.
- 384 Janis Postels, Francesco Ferroni, Huseyin Coskun, Nassir Navab, and Federico Tombari. Sampling-
385 free epistemic uncertainty estimation using approximated variance propagation. In *Proceedings of
386 the IEEE/CVF International Conference on Computer Vision*, 2019.
- 387 Olaf Ronneberger, Philipp Fischer, and Thomas Brox. U-net: Convolutional networks for biomedical
388 image segmentation. In *International Conference on Medical image computing and computer-
389 assisted intervention*. Springer, 2015.
- 390 Olga Russakovsky, Jia Deng, Hao Su, Jonathan Krause, Sanjeev Satheesh, Sean Ma, Zhiheng Huang,
391 Andrej Karpathy, Aditya Khosla, Michael Bernstein, Alexander C. Berg, and Li Fei-Fei. ImageNet
392 Large Scale Visual Recognition Challenge. *International Journal of Computer Vision*, pp. 211–252,
393 2015.
- 394 Mark Sandler, Andrew Howard, Menglong Zhu, Andrey Zhmoginov, and Liang-Chieh Chen. Mo-
395 bilenetv2: Inverted residuals and linear bottlenecks. In *Proceedings of the IEEE Conference on
396 Computer Vision and Pattern Recognition*, 2018.
- 397 Shibani Santurkar, Dimitris Tsipras, Andrew Ilyas, and Aleksander Madry. How does batch normal-
398 ization help optimization? *Advances in Neural Information Processing Systems*, 2018.
- 399 Rulin Shao, Zhouxing Shi, Jinfeng Yi, Pin-Yu Chen, and Cho-Jui Hsieh. On the adversarial robustness
400 of visual transformers. *arXiv preprint arXiv:2103.15670*, 2021.
- 401 Karen Simonyan and Andrew Zisserman. Very deep convolutional networks for large-scale image
402 recognition. In *International Conference on Learning Representations*, 2015.
- 403 Samarth Sinha, Animesh Garg, and Hugo Larochelle. Curriculum by smoothing. *Advances in Neural
404 Information Processing Systems*, 2020.
- 405 Hugo Touvron, Matthieu Cord, Matthijs Douze, Francisco Massa, Alexandre Sablayrolles, and Hervé
406 Jégou. Training data-efficient image transformers & distillation through attention. In *International
407 Conference on Machine Learning*. PMLR, 2021.
- 408 Cristina Vasconcelos, Hugo Larochelle, Vincent Dumoulin, Nicolas Le Roux, and Ross Goroshin.
409 An effective anti-aliasing approach for residual networks. *arXiv preprint arXiv:2011.10675*, 2020.
- 410 Ashish Vaswani, Noam Shazeer, Niki Parmar, Jakob Uszkoreit, Llion Jones, Aidan N Gomez, Łukasz
411 Kaiser, and Illia Polosukhin. Attention is all you need. In *Advances in Neural Information
412 Processing Systems*, 2017.
- 413 Hao Wang, Xingjian Shi, and Dit-Yan Yeung. Natural-parameter networks: A class of probabilistic
414 neural networks. *Advances in Neural Information Processing Systems*, 2016.
- 415 Xiaolong Wang, Ross Girshick, Abhinav Gupta, and Kaiming He. Non-local neural networks. In
416 *Proceedings of the IEEE Conference on Computer Vision and Pattern Recognition*, 2018.
- 417 Yeming Wen, Dustin Tran, and Jimmy Ba. Batchensemble: an alternative approach to efficient
418 ensemble and lifelong learning. In *International Conference on Learning Representations*, 2020.
- 419 Anqi Wu, Sebastian Nowozin, Edward Meeds, Richard E Turner, José Miguel Hernández-Lobato,
420 and Alexander L Gaunt. Deterministic variational inference for robust bayesian neural networks.
421 In *International Conference on Learning Representations*, 2019.
- 422 Saining Xie, Ross Girshick, Piotr Dollár, Zhuowen Tu, and Kaiming He. Aggregated residual
423 transformations for deep neural networks. In *Proceedings of the IEEE Conference on Computer
424 Vision and Pattern Recognition*, 2017.

- 425 Zhewei Yao, Amir Gholami, Kurt Keutzer, and Michael W Mahoney. Pyhessian: Neural networks
426 through the lens of the hessian. In *2020 IEEE International Conference on Big Data (Big Data)*.
427 IEEE, 2020.
- 428 Jaesik Yoon, Taesup Kim, Ousmane Dia, Sungwoong Kim, Yoshua Bengio, and Sungjin Ahn.
429 Bayesian model-agnostic meta-learning. In *Advances in Neural Information Processing Systems*,
430 2018.
- 431 Sergey Zagoruyko and Nikos Komodakis. Wide residual networks. In *BMVC*, 2016.
- 432 Hongyang Zhang, Yaodong Yu, Jiantao Jiao, Eric Xing, Laurent El Ghaoui, and Michael Jordan.
433 Theoretically principled trade-off between robustness and accuracy. In *International Conference*
434 *on Machine Learning*. PMLR, 2019.
- 435 Richard Zhang. Making convolutional networks shift-invariant again. In *International Conference on*
436 *Machine Learning*. PMLR, 2019a.
- 437 Richard Zhang. Official meta-review of making convolutional networks shift-invariant again, 2019b.
438 URL <https://openreview.net/forum?id=Sk1VErR5K7¬eId=rklZnFS-gN>.
- 439 Bolei Zhou, Aditya Khosla, Agata Lapedriza, Aude Oliva, and Antonio Torralba. Learning deep
440 features for discriminative localization. In *Proceedings of the IEEE Conference on Computer*
441 *Vision and Pattern Recognition*, 2016.
- 442 Xueyan Zou, Fanyi Xiao, Zhiding Yu, and Yong Jae Lee. Delving deeper into anti-aliasing in convnets.
443 In *BMVC*, 2020.

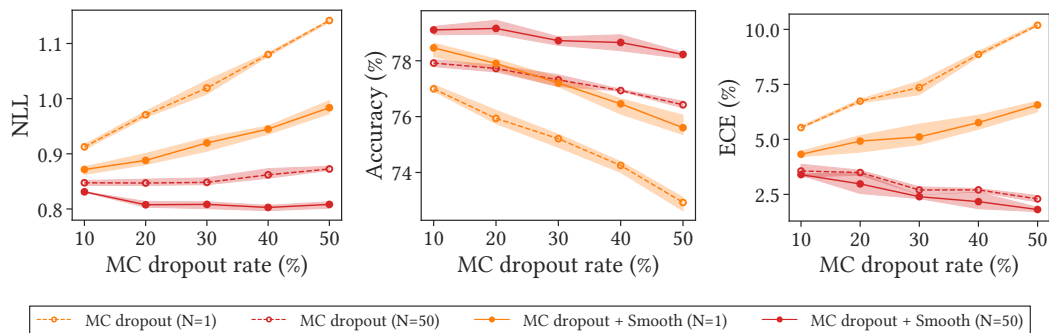


Figure A.1: **Spatial smoothing improves predictive performance at all dropout rates.** As the dropout rate increases, both accuracy and ECE decrease. The performance is optimized when accuracy and uncertainty are balanced.

444 A EXPERIMENTAL SETUP AND DATASETS

445 We obtain the main experimental results with the Intel Xeon W-2123 Processor, 32GB memory, and
 446 a single GeForce RTX 2080 Ti for CIFAR (Krizhevsky et al., 2009) and CamVid (Brostow et al.,
 447 2008). For ImageNet (Russakovsky et al., 2015), we use AMD Ryzen Threadripper 3960X 24-Core
 448 Processor, 256GB memory, and four GeForce RTX 2080 Ti. We conduct ablation studies with four
 449 Intel Intel Broadwell CPUs, 15GB memory, and a single NVIDIA T4. Models are implemented
 450 in PyTorch (Paszke et al., 2019). The detailed configurations of image classification and semantic
 451 segmentation are as follows.

452 A.1 IMAGE CLASSIFICATION

453 We use VGG (Simonyan & Zisserman, 2015), ResNet (He et al., 2016a), pre-activation ResNet (He
 454 et al., 2016a), and ResNeXt (Xie et al., 2017) in image classification. According to the structure
 455 suggested by Zagoruyko & Komodakis (2016), each block of Bayesian NNs contains one MC dropout
 456 layer.

457 NNs are trained using categorical cross-entropy loss and SGD optimizer with initial learning rate of
 458 0.1, momentum of 0.9, and weight decay of 5×10^{-4} . We also use multi-step learning rate scheduler
 459 with milestones at 60, 130, and 160, and gamma of 0.2 on CIFAR, and with milestones at 30, 60,
 460 and 80, and gamma of 0.2 on ImageNet. We train NNs for 200 epochs with batch size of 128 on
 461 CIFAR, and for 90 epochs with batch size of 256 on ImageNet. We start training with gradual warmup
 462 (Goyal et al., 2017) for 1 epoch on CIFAR. Basic data augmentations, namely random cropping and
 463 horizontal flipping, are used. One exception is the training of ResNeXt on ImageNet. In this case, we
 464 use the batch size of 128 and learning rate of 0.05 because of memory limitation.

465 We use hyperparameters that minimizes NLL of ResNet. Table A.1 provides hyperparameters for
 466 deterministic and Bayesian NNs. For fair comparison, models with and without spatial smoothing
 467 share hyperparameters such as MC dropout rate. However, Fig. A.1 shows that spatial smoothing
 468 improves predictive performance of ResNet-18 at all dropout rates on CIFAR-100. The default
 469 ensemble size of MC dropout is 50. We report averages of three evaluations, and error bars in figures
 470 represent min and max values. Standard deviations are omitted from tables for better visualization.
 471 See the source code released on GitHub for other details.

472 A.2 SEMANTIC SEGMENTATION

473 We use U-Net (Ronneberger et al., 2015) in semantic segmentation. Following Bayesian SegNet
 474 (Kendall et al., 2017), Bayesian U-Net contains six MC dropout layers. We add spatial smoothing
 475 before each subsampling layer in U-Net encoder. We use 5 previous predictions and decay rate of
 476 $e^{-0.8}$ for temporal smoothing.

Table A.1: Hyperparameters of models for image classification.

DATASET	MODEL	MC DROPOUT RATE (%)	$ k $	TEMPERATURE
CIFAR-10 & CIFAR-100	VGG	.	.	.
		30	2	10
		.	2	10
	ResNet	30	.	.
		.	2	10
		30	2	10
	Preact-ResNet	.	.	.
		30	2	10
		.	2	10
	ResNeXt	.	.	.
		30	2	10
		.	2	10
ImageNet	ResNet	.	.	.
		5	2	10
		.	2	10
	ResNeXt	.	.	.
		5	2	10
		.	2	10

477 CamVid consists of 720×960 pixels road scene video sequences. We resize the image bilinearly to
 478 360×480 pixels. We use a list reduced to 11 labels by following previous works, e.g. (Kendall & Gal,
 479 2017).

480 NNs are trained using categorical cross-entropy loss and Adam optimizer with initial learning rate of
 481 0.001 and β_1 of 0.9, and β_2 of 0.999. We train NN for 130 epoch with batch size of 3. The learning
 482 rate decreases to 0.0002 at the 100 epoch. Random cropping and horizontal flipping are used for
 483 data augmentation. Median frequency balancing is used to mitigate dataset imbalance. Other details
 484 follow Park et al. (2021).

485 **B ABLATION STUDY**

486 The probabilistic spatial smoothing proposed in this
 487 paper consists of two components: Prob and Blur. This
 488 section explores several candidates for each component
 489 and their properties.

490 **B.1 PROB: FEATURE MAPS TO PROBABILITIES**

491 We define Prob as a composition of an upper-
 492 bounded function and ReLU, a function that imposes
 493 the lower bound of zero. Fig. B.1 shows widely used
 494 upper-bounded functions: $\tanh_\tau(x) = \tau \tanh(x/\tau)$,
 495 $\text{ReLU6}(x) = \min(\max(x, 6), 0)$, and constant scaling
 496 which is x/τ .

497 Table B.1 shows the predictive performance improve-
 498 ment by Prob with various upper-bounded functions on

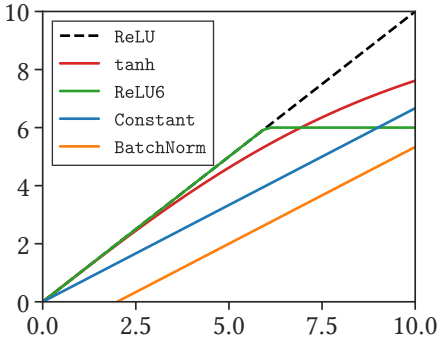


Figure B.1: Upper-bounded functions as a candidates of Prob.

Table B.1: We use tanh as the default for Prob based on the predictive performance of MC dropout for CIFAR-100 with various Probs.

MODEL	SMOOTH	NLL	Acc (%)	ECE (%)
VGG-16	.	1.133 (-0.000)	68.8 (+0.0)	3.66 (+0.00)
	ReLU \circ <u>tanh</u>	1.064 (-0.069)	70.4 (+1.6)	2.99 (-0.67)
	ReLU \circ <u>ReLU6</u>	1.093 (-0.040)	69.8 (+1.0)	4.26 (+0.60)
	ReLU \circ <u>Constant</u>	0.995 (-0.138)	72.5 (+3.7)	2.11 (-1.55)
	Blur	0.985 (-0.000)	72.4 (+0.0)	1.77 (+0.00)
	Blur \circ ReLU \circ <u>tanh</u>	0.984 (-0.001)	72.7 (+0.3)	2.07 (+0.30)
	Blur \circ ReLU \circ <u>ReLU6</u>	0.982 (-0.003)	72.5 (+0.1)	1.84 (+0.07)
	Blur \circ ReLU \circ <u>Constant</u>	0.991 (+0.005)	72.9 (+0.5)	1.03 (-0.74)
VGG-19	.	1.215 (-0.000)	67.3 (+0.0)	6.37 (+0.00)
	ReLU \circ <u>tanh</u>	1.131 (-0.084)	69.2 (+1.9)	5.23 (-1.14)
	ReLU \circ <u>ReLU6</u>	1.166 (-0.049)	68.3 (+1.0)	6.44 (-0.06)
	ReLU \circ <u>Constant</u>	0.997 (-0.218)	72.5 (+5.2)	1.09 (-5.29)
	Blur	1.039 (-0.000)	71.1 (+0.0)	3.12 (+0.00)
	Blur \circ ReLU \circ <u>tanh</u>	1.034 (-0.005)	71.3 (+0.2)	3.31 (+0.19)
	Blur \circ ReLU \circ <u>ReLU6</u>	1.038 (-0.002)	71.3 (+0.2)	3.84 (+0.72)
	Blur \circ ReLU \circ <u>Constant</u>	0.995 (-0.045)	72.3 (+1.2)	1.41 (-1.71)
ResNet-18	.	0.848 (-0.000)	77.3 (+0.0)	3.01 (+0.00)
	ReLU \circ <u>tanh</u>	0.838 (-0.010)	77.7 (+0.4)	2.92 (-0.08)
	ReLU \circ <u>ReLU6</u>	0.844 (-0.004)	77.4 (+0.1)	2.74 (-0.27)
	ReLU \circ <u>Constant</u>	0.825 (-0.023)	77.7 (+0.4)	1.87 (-1.14)
	Blur	0.806 (-0.000)	78.6 (+0.0)	2.56 (+0.00)
	Blur \circ ReLU \circ <u>tanh</u>	0.801 (-0.005)	78.9 (+0.3)	2.56 (-0.01)
	Blur \circ ReLU \circ <u>ReLU6</u>	0.805 (-0.001)	78.9 (+0.2)	2.59 (+0.03)
	Blur \circ ReLU \circ <u>Constant</u>	0.811 (+0.005)	78.5 (-0.2)	1.84 (-0.72)
ResNet-50	.	0.822 (-0.000)	79.1 (+0.0)	6.63 (+0.00)
	ReLU \circ <u>tanh</u>	0.812 (-0.010)	79.3 (+0.2)	6.74 (+0.11)
	ReLU \circ <u>ReLU6</u>	0.799 (-0.023)	79.4 (+0.3)	6.71 (+0.08)
	ReLU \circ <u>Constant</u>	0.788 (-0.034)	79.6 (+0.5)	5.22 (-1.41)
	Blur	0.798 (-0.000)	80.0 (+0.0)	7.21 (+0.00)
	Blur \circ ReLU \circ <u>tanh</u>	0.800 (+0.002)	80.1 (+0.1)	7.25 (+0.04)
	Blur \circ ReLU \circ <u>ReLU6</u>	0.800 (+0.002)	80.2 (+0.2)	7.30 (+0.09)
	Blur \circ ReLU \circ <u>Constant</u>	0.779 (-0.019)	80.4 (+0.4)	5.81 (-1.40)

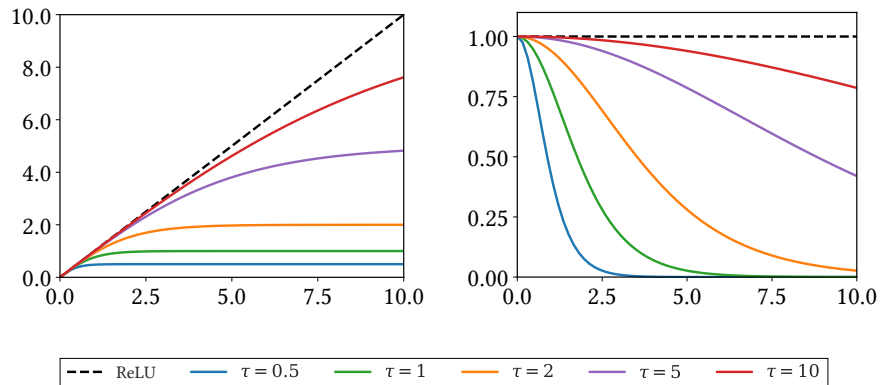


Figure B.2: Temperature-scaled \tanh s (left) and their first derivatives (right) for different temperatures.

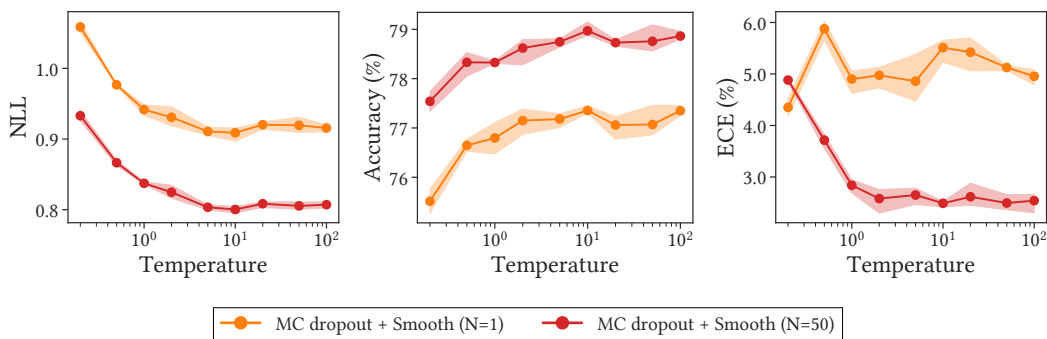
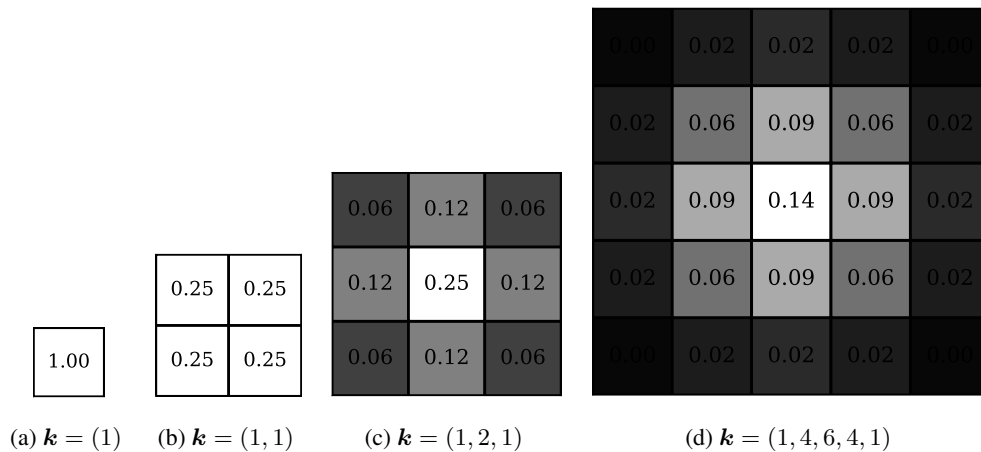


Figure B.3: The temperature controls the trade-off between accuracy and uncertainty. The accuracy increases as the temperature increases, but predictions become more overconfident.

499 CIFAR-100. In this experiment, we use models with MC dropout, and $\tau = 5$ for constant scaling. The
 500 results indicate that upper-bounded functions with ReLU tend to improve accuracy and uncertainty
 501 at the same time. In addition, they show that `Prob` and `Blur` are complementary. The best results
 502 are obtained when using both `Prob` and `Blur`. For the main experiments, we use the composition
 503 of \tanh_τ and ReLU as `Prob`, because the hyperparameter of constant scaling is highly dependent on
 504 dataset and model.

505 **Temperature.** The characteristics of temperature-scaled \tanh depends on τ . Figure B.2 plots
 506 \tanh_τ and their first derivatives with various temperatures. As shown in this figure, \tanh_τ has a
 507 couple of useful properties. First, \tanh_τ has an upper bound of τ . Second, the first derivative of
 508 \tanh_τ at $x = 0$ does not depend on τ .

509 Fig. B.3 shows the predictive performance of ResNet-18 with MC dropout and spatial smoothing for
 510 the temperature on CIFAR-100. In this figure, the accuracy increases as the temperature increases. In
 511 terms of ECE, NN predicts more underconfident results as τ decreases. It is a misinterpretation that
 512 the result is overconfident at low τ because ECE is high. By definition, ECE relies on the absolute
 513 value of the difference between confidence and accuracy. In this example, at low τ , the accuracy is
 514 greater than the confidence, which leads to a high ECE. Moreover, at $\tau = 0.2$, ECE with $N = 50$ is
 515 greater than that with $N = 1$, which means that the result is severely underconfident. NLL, a metric
 516 representing both accuracy and uncertainty, is minimized when the accuracy and the uncertainty are
 517 balanced. In conclusion, we set the default value of τ to 10.

Figure B.4: **Kernels for Blur**. Brighter background indicates higher importance.Table B.2: **The optimal shape of the blur kernel is model-dependent**. We measure the predictive performance of MC dropout using spatial smoothing with various size of Blur kernels on CIFAR-100.

MODEL	$ \mathbf{k} $	NLL	ACC (%)	ECE (%)
VGG-16	1	1.087 (-0.000)	69.8 (+0.0)	3.43 (-0.00)
	2	1.034 (-0.053)	71.4 (+1.6)	1.06 (-2.37)
	3	0.986 (-0.101)	72.7 (+2.9)	1.03 (-2.40)
	5	1.018 (-0.069)	72.0 (+2.2)	1.32 (-2.11)
VGG-19	1	1.096 (-0.000)	69.8 (+0.0)	4.74 (-0.00)
	2	1.071 (-0.025)	70.4 (+0.6)	2.15 (-2.59)
	3	1.026 (-0.070)	71.9 (+2.1)	2.56 (-2.18)
	5	1.032 (-0.064)	71.6 (+1.8)	2.16 (-2.58)
ResNet-18	1	0.840 (-0.000)	77.6 (+0.0)	2.63 (-0.00)
	2	0.801 (-0.039)	78.9 (+1.4)	2.56 (-0.07)
	3	0.822 (-0.018)	78.7 (+1.1)	2.86 (-0.23)
	5	0.837 (-0.003)	78.4 (+0.8)	3.05 (-0.42)
ResNet-50	1	0.814 (-0.000)	79.5 (+0.0)	6.56 (-0.00)
	2	0.806 (-0.008)	80.0 (+0.5)	7.35 (+0.79)
	3	0.796 (-0.019)	79.9 (+0.4)	7.38 (+0.82)
	5	0.816 (+0.001)	79.4 (-0.1)	7.38 (+0.82)

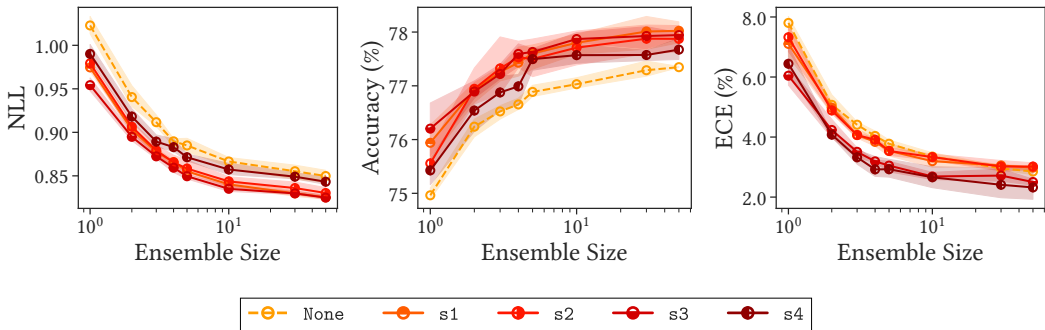


Figure B.5: **Spatial smoothing close to the last layer (s3) significantly improves performance.** We report predictive performance of ResNet-18 with *one* spatial smoothing after each stage on CIFAR-100. None indicates vanilla MC dropout.

518 B.2 BLUR: AVERAGING NEIGHBORING PROBABILITIES

519 Blur is a depth-wise convolution with a kernel. The kernel given by Eq. (8) is derived from various
 520 \mathbf{k} s such as $\mathbf{k} \in \{(1), (1, 1), (1, 2, 1), (1, 4, 6, 4, 1)\}$. In these examples, if $|\mathbf{k}|$ is 1, Blur is identity.
 521 If $|\mathbf{k}|$ is 2, Blur is a box blur, which is used in the main experiments. If $|\mathbf{k}|$ is 3 or 5, Blur is an
 522 approximated Gaussian blur.

523 Table B.2 shows predictive performance of models using spatial smoothing with the kernels on
 524 CIFAR-100. This results show that *most kernels improve both accuracy and uncertainty.* However,
 525 the most effective kernel size depends on the model.

526 B.3 POSITION OF SPATIAL SMOOTHING.

527 As shown in Fig. 5, the magnitude of uncertainty tends to increase as the depth increases. Therefore,
 528 we expect that spatial smoothing close to the output layer will mainly drive performance improvement.

529 We investigate the predictive performance of models with MC dropout using only *one* spatial smooth-
 530 ing layer. Figure B.5 shows the predictive performance of ResNet-18 with one spatial smoothing after
 531 each stage on CIFAR-100. The results suggest that spatial smoothing after s3 is the most important
 532 for improving performance. Surprisingly, spatial smoothing after s4 is the least important. This is
 533 because GAP, the most extreme case of spatial smoothing, already exists there.

534 C REVISITING PRIOR WORKS

535 As mentioned in Section 2, prior works—namely, GAP, pre-activation, and ReLU6—are spacial cases
 536 of spatial smoothing. This section discusses them in detail.

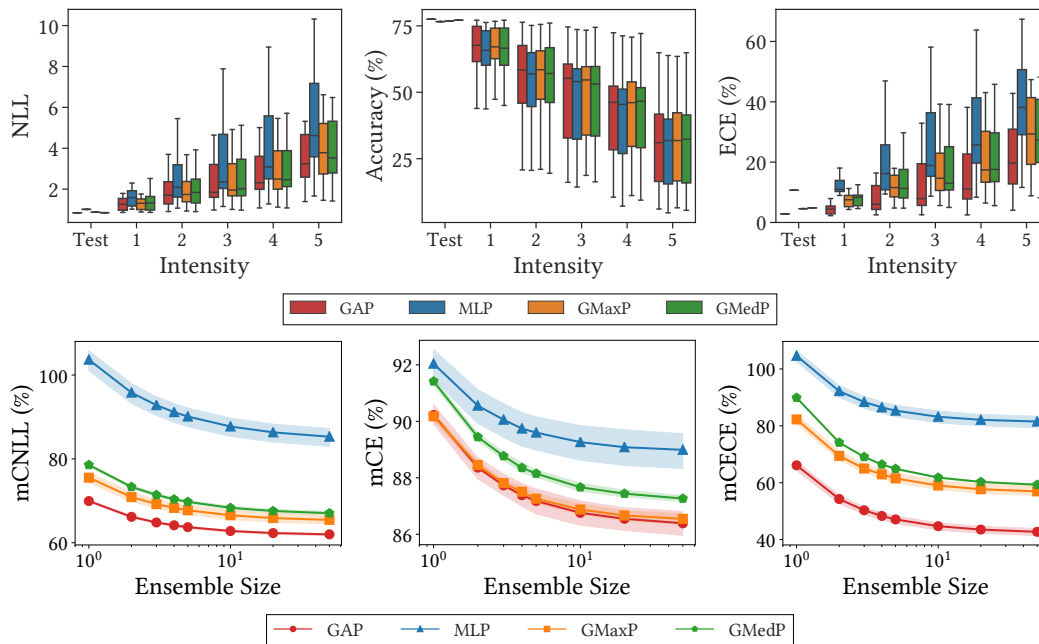
537 C.1 GLOBAL AVERAGE POOLING

538 The composition of GAP and a fully connected layer is the most popular classifier in classification
 539 tasks. The original motivation and the most widely accepted explanation for the success is that *GAP*
 540 *classifier prevents overfitting because it uses significantly fewer parameters than MLP* (Lin et al.,
 541 2014). To verify this claim, we measure the predictive performance of MLP, GAP, and global max
 542 pooling (GMaxP), a classifier that uses the same number of parameters as GAP, on training dataset.

543 **Predictive performance.** Table C.1 shows the experimental results on the training and the test
 544 dataset of CIFAR-100, suggesting that the explanation is poorly supported. On *both* the training
 545 and the test dataset, most predictive performance of MLP is worse than that of GAP. It is a counter-
 546 intuitive result meaning that *MLP do not overfit the training dataset.* In addition, the performance
 547 improvement by GAP is remarkable in VGG, which has irregular loss landscape. The predictive

Table C.1: **MLP classifier does not overfit training dataset**, i.e., GAP does not regularize NNs. We provide predictive performance of MC dropout with various classifiers on CIFAR-100. ERR is error.

MODEL	CLASSIFIER	TRAIN			TEST		
		NLL	ERR (%)	ECE (%)	NLL	ACC (%)	ECE (%)
VGG-16	GAP	0.0852	0.461	6.75	1.030	72.3	3.24
	MLP	0.5492	13.1	13.8	1.133	68.8	3.66
	GMaxP	0.0846	0.470	6.67	1.050	72.2	3.60
	GMedP	0.0867	0.501	6.80	1.042	72.2	3.35
VGG-19	GAP	0.1825	2.50	10.4	1.035	71.9	1.46
	MLP	0.7144	17.7	14.8	1.215	67.3	6.37
	GMaxP	0.1939	2.85	10.6	1.063	71.5	2.10
	GMedP	0.1938	2.80	10.6	1.051	71.7	1.70
ResNet-18	GAP	0.0124	0.0287	1.19	0.841	77.5	2.92
	MLP	0.0076	0.0347	7.22	1.040	74.8	9.55
	GMaxP	0.0113	0.0233	1.41	0.905	76.3	5.23
	GMedP	0.0156	0.0347	1.46	0.889	76.4	5.03
ResNet-50	GAP	0.0061	0.0220	0.48	0.822	79.1	6.63
	MLP	0.0071	0.0370	8.53	1.029	76.9	11.8
	GMaxP	0.0074	0.0313	1.09	0.887	77.2	5.67
	GMedP	0.0053	0.0287	0.47	0.849	78.5	6.29

Figure C.1: **GAP classifier improves not only the predictive performance on clean dataset but also the robustness.** We measure the predictive performance of ResNet-18 using MC dropout with classifiers on CIFAR-100-C.

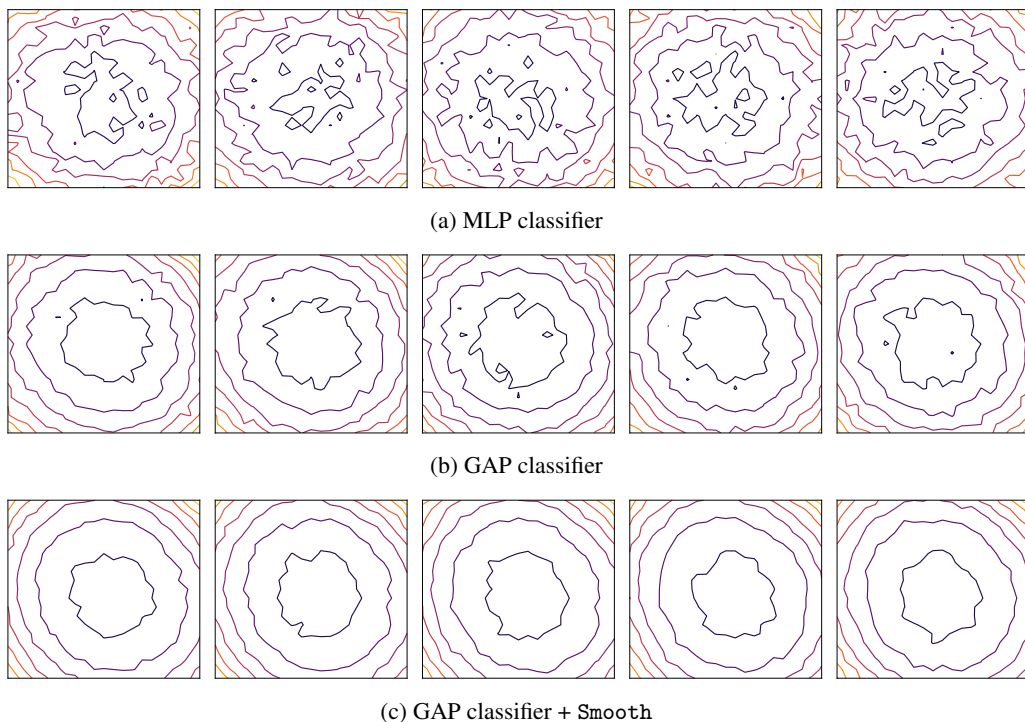


Figure C.2: **GAP and spatial smoothing flatten the loss landscapes.** We visualize the loss landscape sequences of ResNet-18 with MC dropout on CIFAR-100. Although each sequence shares the bases, it fluctuates due to the randomness of the MC dropout.

548 performance of GMaxP is better than that of MLP, but worse than that of GAP. This shows that using
 549 fewer parameters partially helps to improve predictive performance; however, it is insufficient to
 550 explain the predictive performance improvement by GAP. Finally, global median pooling (GMedP)
 551 provides better predictive performance than GMaxP. It implies that using other noise reduction
 552 methods instead of average pooling helps to improve predictive performance.

553 **Robustness.** To evaluate the robustness of the classifiers, we measure the predictive performance of
 554 ResNet-18 using MC dropout with the classifiers on CIFAR-100-C. [Figure C.1](#) shows the experimental
 555 results. This figure suggests that MLP is not robust against data corruption, as we would expect. In
 556 terms of accuracy, the robustness of GMaxP and GMedP is relatively comparable to that of GAP;
 557 however, in terms of uncertainty, *GAP is the most robust*. These are consistent results with other
 558 spatial smoothing experiments.

559 **Loss landscape visualization.** To understand the mechanism of GAP performance improvement,
 560 we investigate the loss landscape. [Figure C.2](#) shows the loss landscape sequences of ResNet with
 561 MC dropout. In this figure, each sequence shares the bases, but they fluctuate due to the randomness
 562 of the MC dropout. [Figure C.2a](#) is the loss landscape of the model using MLP classifier instead of
 563 GAP classifier. The loss landscape is chaotic and irregular, resulting in hindering and destabilizing
 564 NN optimization. [Fig. C.2b](#) is loss landscape sequence of ResNet with GAP classifier. Since GAP
 565 ensembles all of the feature map points at the last stage, it flattens and stabilizes the loss landscape.
 566 Likewise, as shown in [Fig. C.2c](#), spatial smoothing layers at the end of all stages also flattens and
 567 stabilizes the loss landscape.

568 **Hessian eigenvalue spectra.** To evaluate the smoothness of the loss landscapes quantitatively,
 569 we also investigate their Hessians at the optimized weights. In particular, we calculate Hessian
 570 eigenvalue spectra ([Ghorbani et al., 2019](#)), distributions of Hessian eigenvalues, to show how spatial
 571 smoothing helps NN optimization. To this end, we try to use stochastic Lanczos quadrature algorithm

572 implemented by Yao et al. (2020). However, the problem is that the model with MLP classifier
573 requires a lot of memory while the algorithm is memory inefficient.

574 In the training phase, we calculate the mean gradients with respect to mini-batches, rather than the
575 entire dataset. Therefore, it may be reasonable to investigate the properties of the Hessian “mini-
576 batch-wisely”. For that purpose, we propose a method, *Hessian max eigenvalue spectra*, that evaluates
577 the distribution of “Hessian’s maximum eigenvalues for one mini-batch”. We use power iteration to
578 produce only the greatest eigenvalue of the Hessian. This algorithm is easy to implement and requires
579 significantly less memory and computational cost, compared with stochastic Lanczos quadrature
580 with respect to entire dataset. With this method, we can investigate the Hessian of NNs with MLP
581 classifiers, which would require a lot of GPU memory.

582 Figure 7 shows the Hessian max eigenvalue spectra of GAP classifier models with and without spatial smoothing layers. As Li et al.
583 (2018); Foret et al. (2020) and Appendix D.3 pointed out, Hessian
584 eigenvalue outliers disturb NN training. This figure explicitly show
585 that the GAP and spatial smoothing reduce the magnitude of the
586 Hessian eigenvalues and suppress the outliers, which leads to the
587 same result as the previous visualizations: GAP as well as spatial
588 smoothing smoothen the loss landscape. In conclusion, *averag-
589 ing feature map points tends to help neural network optimization
590 by smoothing, flattening, and stabilizing the loss landscape*. We
591 observe a similar phenomenon for deterministic NNs. We also
592 evaluate the Hesse eigenvalue spectrum as shown in Fig. C.3, and
593 it leads to the same conclusion.
594

595 In these experiments, we use MLP incorporating dropout layers
596 with a rate of 50% as the classifier. Since the dropout is one of
597 the factors that makes MLP underfit the training dataset, we also
598 evaluate MLP using dropouts with a rate of 0%. Nevertheless, the
599 results still shows that the predictive performance of MLP is worse
600 than that of GAP on the training dataset. Moreover, it severely degrades predictive performance of
601 ResNet on the test dataset.

602 C.2 PRE-ACTIVATION

603 He et al. (2016b) experimentally showed that the pre-activation arrangement, in which the activation
604 ReLU ◦ BatchNorm is placed before the convolution, improves the accuracy of ResNet. Since γ s of
605 most BatchNorms in CNNs are near-zero (Frankle et al., 2021), BatchNorms reduce the magnitude
606 of feature maps. As shown in Fig. B.1, constant scaling is a non-trainable BatchNorm with no
607 bias, and it also reduces the magnitude of feature map. In Table B.1, we show that constant scaling
608 improves predictive performance. Considering the similarity between Prob with constant scaling and
609 conventional activation, i.e., the similarity between ReLU ◦ ConstantScaling and ReLU ◦ BatchNorm,
610 we find that the pre-activation arrangement improves uncertainty as well as accuracy, because
611 convolutions act as a Blur.

612 To show this, we change the post-activation of all layers to pre-activation, and measure the predictive
613 performance. For ResNet, we follow the original paper by He et al. (2016b). Table C.2 shows
614 the predictive performance of models with pre-activation. The results suggests that pre-activation
615 improves both accuracy and uncertainty in most cases. For deterministic VGG-19, pre-activation
616 significantly degrades accuracy but improves NLL. In conclusion, they imply that pre-activation is a
617 special case of spatial smoothing.

618 Santurkar et al. (2018) argued that BatchNorm helps in optimization by flattening the loss landscape.
619 We show that spatial smoothing flattens and smoothen the loss landscape, which is a consistent
620 explanation. It will be interesting to investigate if BatchNorm helps in ensembling feature maps.

621 C.3 RELU6

622 ReLU6 was experimentally introduced to improve predictive performance (Krizhevsky & Hinton,
623 2010). Sandler et al. (2018) used “ReLU6 as the non linearity because of its robustness when used

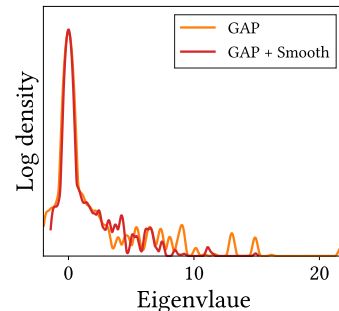


Figure C.3: **Spatial smoothing suppress eigenvalue outliers.** We provide Hessian eigenvalue spectra of ResNet-18 with MC dropout on CIFAR-100. See also Fig. 7.

Table C.2: **Pre-activation arrangement improves uncertainty as well as accuracy.** We measure the predictive performance of models with pre-activation arrangement on CIFAR-100.

MODEL	MC DROPOUT	PRE-ACT	NLL	ACC (%)	ECE (%)
VGG-16	.	.	2.047 (-0.000)	71.6 (+0.0)	19.2 (-0.0)
	.	✓	1.827 (-0.219)	72.5 (+0.9)	19.8 (+0.6)
	✓	.	1.133 (-0.000)	68.8 (+0.0)	3.66 (-0.00)
	✓	✓	1.036 (-0.096)	71.7 (+2.9)	3.55 (-0.11)
VGG-19	.	.	2.016 (-0.000)	67.6 (+0.0)	21.2 (-0.0)
	.	✓	1.799 (-0.217)	64.4 (-3.2)	17.2 (-4.0)
	✓	.	1.215 (-0.000)	67.3 (+0.0)	6.37 (-0.00)
	✓	✓	1.084 (-0.131)	70.1 (+3.7)	4.23 (-2.14)
ResNet-18	.	.	0.983 (-0.000)	77.1 (+0.0)	7.75 (-0.00)
	.	✓	0.934 (-0.049)	77.6 (+0.5)	8.04 (+0.29)
	✓	.	0.937 (-0.000)	76.9 (+0.0)	5.11 (-0.00)
	✓	✓	0.872 (-0.065)	77.6 (+0.7)	5.53 (+0.42)
ResNet-50	.	.	0.880 (-0.000)	79.0 (+0.0)	8.35 (-0.00)
	.	✓	0.870 (-0.010)	79.4 (+0.4)	8.27 (-0.08)
	✓	.	0.831 (-0.000)	78.6 (+0.0)	6.06 (-0.00)
	✓	✓	0.819 (-0.012)	79.5 (+0.9)	6.29 (+0.23)

624 with low-precision computation”. In Table B.1, we show that ReLU6s at the end of stages helps to
625 ensemble spatial information by transforming the feature map to Bernoulli distributions. Since spatial
626 smoothing improves robustness against data corruption, it seems reasonable that ReLU6 is robust to
627 low-precision computation. A more abundant investigation into this topic is promising future works.

628 We measure the predictive performance of NNs using all activations as ReLU6 instead of ReLU.
629 However, in contrast to the results in Table B.1, the results are not consistent. We speculate that the
630 reason is that a lot of ReLU6s overly regularize NNs.

631 D EXTENDED ANALYSIS OF HOW SPATIAL SMOOTHING WORKS

632 This section provides further explanation of the analysis in Section 2.2.

633 D.1 NEIGHBORING FEATURE MAPS IN CNNs ARE SIMILAR

634 This work exploits the spatial consistency of feature maps, i.e., *neighboring feature maps in CNNs*
635 *are similar*. Below, we theoretically and empirically prove the spatial consistency. Moreover, this
636 spatial consistency of feature maps holds even if the input data is spatially inconsistent.

Consider a single-layer convolutional neural network with one channel:

$$y_i = [\mathbf{w} * \mathbf{x}]_i \tag{9}$$

$$= \sum_{l=1}^k w_l x_{i-l+1} \tag{10}$$

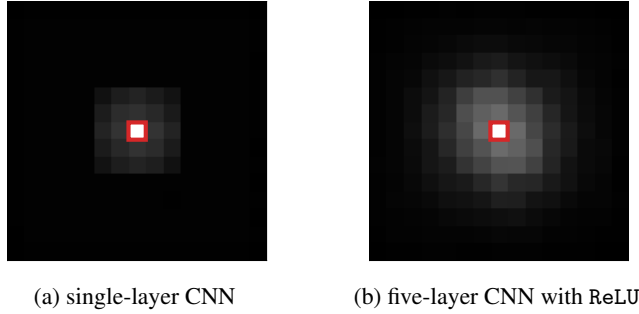


Figure D.1: **Neighboring feature map points in CNNs are similar, even if input values are iid.** We provide covariances of feature map points with respect to the center feature map (in the red square). Input values are Gaussian random noise. *Left*: A single convolutional layer correlates the target feature map with another feature map that is 3 pixels away, since the kernel size is 3×3 . *Right*: A deep CNN more strongly correlates neighboring feature maps.

where $*$ is convolution operator with a kernel of size k , \mathbf{y} is feature map output, \mathbf{w} is kernel weight, and \mathbf{x} is input *random variable*. Then, the covariance of two neighboring feature maps is:

$$\text{Cov}(y_i, y_{i+1}) = \text{Cov}\left(\sum_{l=1}^k w_l x_{i-l+1}, \sum_{m=1}^k w_m x_{i-m+2}\right) \quad (11)$$

$$= \sum_{l=1}^k \sum_{m=1}^k w_l w_m \text{Cov}(x_{i-l+1}, x_{i-m+2}) \quad (12)$$

$$= \sum_{l=1}^{k-1} w_l w_{l+1} \sigma^2(x_{i-l+2}) + \dots \quad (13)$$

637 where $\sigma^2(x_{i-l+1})$ is the variance of x_{i-l+1} . Therefore, $\text{Cov}(\mathbf{y}_i, \mathbf{y}_{i+1})$ is non-zero for randomly
 638 initialized weights. If \mathbf{x} is *iid*, i.e., $\text{Cov}(x_i, x_j) = \delta_{ij} \sigma^2(x_i)$ where δ_{ij} is the Kronecker delta, the
 639 remainders in Eq. (13) vanish.

For example, the covariance of two neighboring feature map points in a CNN with a kernel size of 3 is:

$$\begin{aligned} \text{Cov}(y_1, y_2) &= w_1 w_1 \text{Cov}(x_1, x_2) + w_1 w_2 \text{Cov}(x_1, x_3) + w_1 w_3 \text{Cov}(x_1, x_4) \\ &\quad + w_2 w_1 \text{Cov}(x_2, x_2) + w_2 w_2 \text{Cov}(x_2, x_3) + w_2 w_3 \text{Cov}(x_2, x_4) \\ &\quad + w_3 w_1 \text{Cov}(x_3, x_2) + w_3 w_2 \text{Cov}(x_3, x_3) + w_3 w_3 \text{Cov}(x_3, x_4) \end{aligned} \quad (14)$$

When x_i is *iid*, the covariance is:

$$\text{Cov}(y_1, y_2) = w_1 w_2 \sigma^2(x_2) + w_2 w_3 \sigma^2(x_3) \quad (15)$$

640 Since it is non-zero, the neighboring feature maps y_1 and y_2 are correlated.

641 **Experiment.** To demonstrate the spatial consistency of feature maps empirically, we provide
 642 feature map covariances of randomly initialized single-layer CNN and five-layer CNN with ReLU
 643 non-linearity. In this experiment, the input values are Gaussian random noises. As shown in Fig. D.1a,
 644 one convolutional layer correlates neighboring feature map points. Fig. D.1b shows that multiple
 645 convolutional layers correlate one feature map with distant feature maps. Moreover, the feature maps
 646 in deep CNNs have a stronger relationship with neighboring feature maps.

647 D.2 ENSEMBLE FILTERS HIGH-FREQUENCY SIGNALS

Following the notation of Eq. (3), the ensemble is convolution of importance π and prediction p :

$$\pi * p \quad (16)$$

where $\pi_{i,j} = \pi(\mathbf{x}_i|\mathbf{x}_j)$ and $\mathbf{p}_i = p(\mathbf{y}|\mathbf{x}_i, \mathbf{w}_i)$. To show that this ensemble is low-pass filter, we apply the convolution N times:

$$\underbrace{\pi * \dots * \pi}_{N \text{ times}} * \mathbf{p} \quad (17)$$

648 Since π is probability, i.e., $\sum_i \pi_{i,j} = 1$, $\pi * \dots * \pi$ is the probability for the sum of N random
 649 variables from π , i.e., $\phi + \dots + \phi \sim \pi * \dots * \pi$ where $\phi \sim \pi$. By definition, an operator is
 650 low-pass filter if and only if the high frequency component vanishes when the operator is applied
 651 infinitely. Therefore, ensemble with π is low-pass filter because $\mathbf{Var}(\phi + \dots + \phi) = N \mathbf{Var}(\phi)$ and
 652 $\mathcal{F}[\pi * \dots * \pi * \mathbf{p}] = \mathcal{F}[\pi * \dots * \pi] \mathcal{F}[\mathbf{p}]$ where \mathcal{F} is Fourier transform.

653 **Experiment.** Since blur filter is low-pass filter, probabilistic spatial smoothing is also low-pass
 654 filter. In Section 2.2, at the end of the stage 1, we show that MC dropout adds high-frequency noise to
 655 feature maps, and spatial smoothing effectively removes it. As shown in Fig. D.2, we observe the
 656 same phenomena at other stages.

657 In addition, Fig. 6c shows that CNNs are vulnerable to high-frequency random noise. Interestingly, it
 658 also shows that CNNs are robust against noise with frequencies from 0.6π to 0.8π , corresponding to
 659 approximately 3 pixel periods. Since the receptive fields of convolutions are 3×3 , the noise with a
 660 period smaller than the size is averaged out by convolutions. For the same reason, convolutions are
 661 particularly vulnerable against the noise with a frequency of 0.3π , corresponding to a period of 6
 662 pixel.

663 D.3 RANDOMNESS SHARPENS LOSS LANDSCAPE, AND ENSEMBLE SMOOTHENS IT

664 We show that the randomness of BNNs hinder and destabilize NN training because it causes the loss
 665 landscape and its gradient to fluctuate from moment to moment. In other words, the randomness,
 666 such as dropout, sharpens the loss landscape.

To show the claim theoretically, we use Foret et al. (2020)’s definition of sharpness with respect to training dataset \mathcal{D} :

$$\text{sharpness}_\rho = \max_{\delta \mathbf{w} \leq \rho} \mathcal{L}_{\mathcal{D}}(\mathbf{w} + \delta \mathbf{w}) - \mathcal{L}_{\mathcal{D}}(\mathbf{w}) \quad (18)$$

667 where $\mathcal{L}_{\mathcal{D}}$ is NLL loss, \mathbf{w} is NN weight, $\delta \mathbf{w}$ is small weight perturbation, and ρ is neighborhood
 668 radius. Therefore, as dropout rate—and the magnitude of $\delta \mathbf{w}$ —increases, the sharpness increases.

We next calculate the sharpness more rigorously. Let $p_i \in (0, 1]$ be a confidence of one NN prediction, and $\bar{p}^{(N)}$ be a confidence of N ensemble, i.e., $\bar{p}^{(N)} = \frac{1}{N} \sum_{i=1}^N p_i$. Then, the variance of the NLL loss is:

$$\mathbb{V}[\mathcal{L}] = \mathbb{V} \left[\frac{1}{|\mathcal{D}|} \sum_{\mathcal{D}} -\log \bar{p}^{(N)} \right] \quad (19)$$

$$= \frac{1}{|\mathcal{D}|} \mathbb{V} \left[-\log \bar{p}^{(N)} \right] \quad (20)$$

$$\simeq \frac{1}{|\mathcal{D}|} \mathbb{V} \left[-\log \mu + \left(1 - \frac{\bar{p}^{(N)}}{\mu} \right) \right] \quad (21)$$

$$= \frac{1}{|\mathcal{D}|} \mathbb{V} \left[-\frac{\bar{p}^{(N)}}{\mu} \right] \quad (22)$$

$$= \frac{1}{N} \frac{\mathbb{V}[p_i]}{\mu^2 |\mathcal{D}|} \quad (23)$$

$$= \frac{1}{N} \frac{\sigma_{\text{pred}}^2}{\mu^2 |\mathcal{D}|} \quad (24)$$

where $\mu = \bar{p}^{(\infty)}$ and σ_{pred}^2 is predictive variance of confidence. We use the formula $\mathbb{V} \left[\frac{1}{N} \sum_{i=1}^N \xi \right] = \frac{1}{N} \mathbb{V}[\xi]$ for arbitrary random variable ξ , and we take the first-order Taylor expansion with an assump-

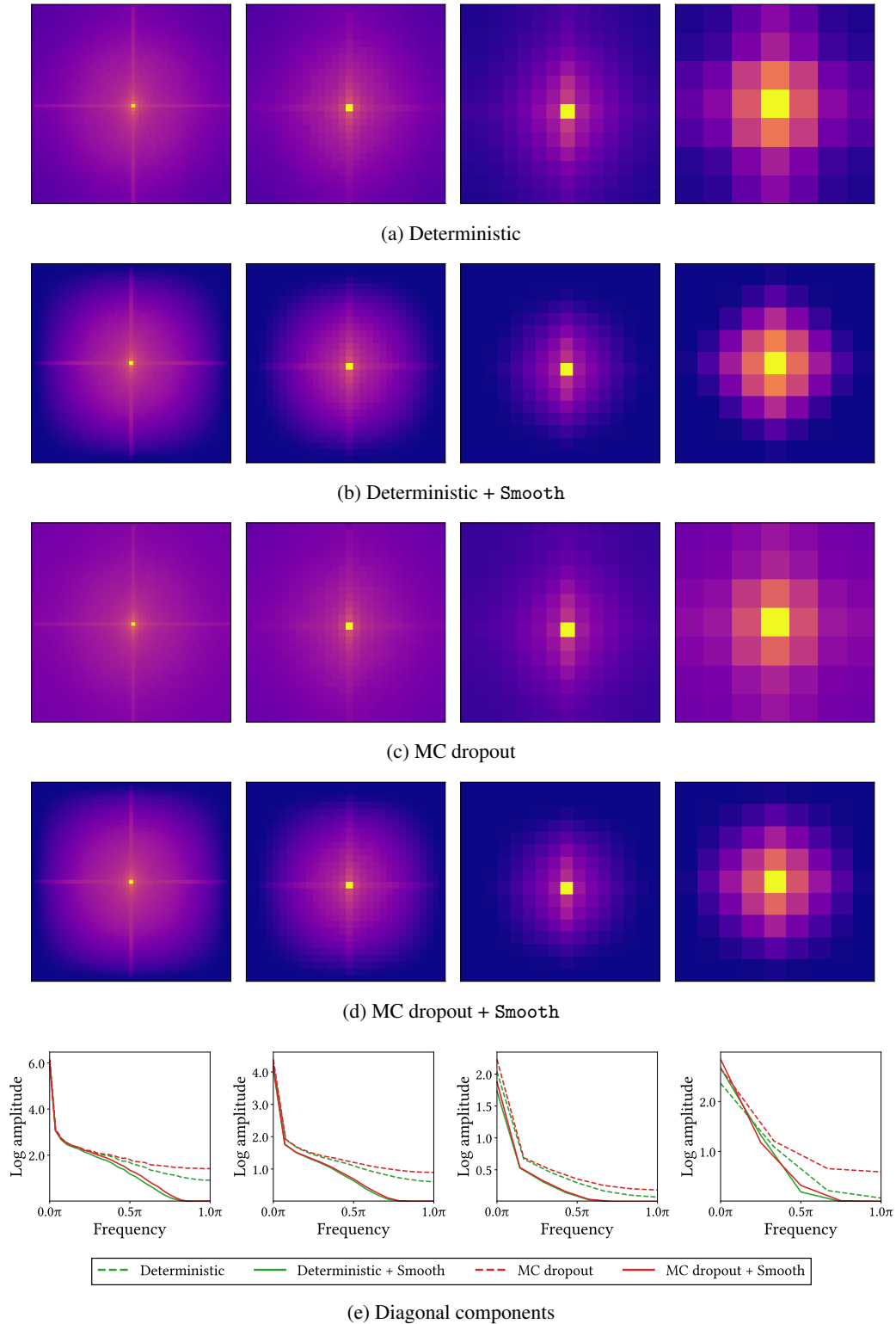


Figure D.2: **Spatial smoothing filters high-frequency signals including MC dropout noise.** We present average feature maps of ResNet-50 on ImageNet in frequency space by using Fourier transform. Each column corresponds to feature maps at stage 1 to 4.

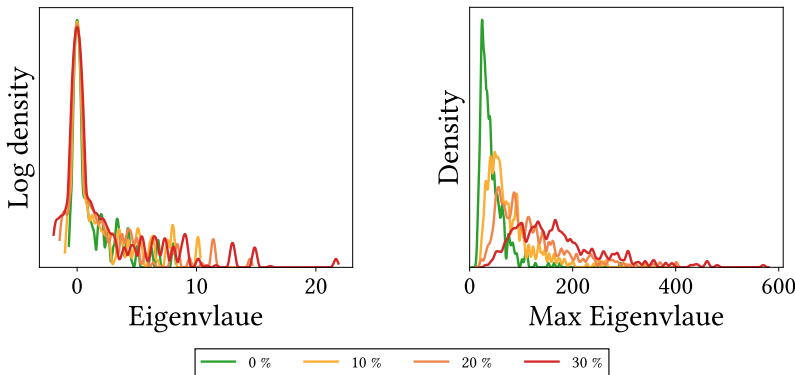


Figure D.3: **Randomness due to MC dropout sharpens the loss function.** We provide Hessian eigenvalue (*left*) and Hessian max eigenvalue spectra (*right*) of ResNet-18 on CIFAR-100.

tion $\bar{p}^{(N)} \simeq \mu$ in Eq. (21). Therefore, the approximated sharpness is:

$$\text{sharpness}_\rho^2 \simeq \frac{1}{N} \frac{\sigma_{\text{pred}}^2}{\mu^2 |\mathcal{D}|} \quad (25)$$

669 In conclusion, *the variance of NLL, (the square of) the sharpness, is proportional to the variance of*
 670 *predictions σ_{pred}^2 and inversely proportional to the ensemble size N .* As the ensemble size increases
 671 in the training phase, the loss landscape becomes smoother. Flat loss landscape results in better
 672 predictive performance and generalization (Foret et al., 2020).

Here, we only consider model uncertainty for the sake of simplicity. Extending the formulations to data uncertainty is straightforward. The predictive distribution of data-complemented BNN inference (Park et al., 2021) is:

$$p(\mathbf{y}|\mathcal{S}, \mathcal{D}) = \int p(\mathbf{y}|\mathbf{x}, \mathbf{w})p(\mathbf{x}|\mathcal{S})p(\mathbf{w}|\mathcal{D})d\mathbf{x}d\mathbf{w} \quad (26)$$

$$= \int p(\mathbf{y}|\mathbf{z})p(\mathbf{z}|\mathcal{S}, \mathcal{D})d\mathbf{z} \quad (27)$$

673 where \mathcal{S} is proximate data distribution, $\mathbf{z} = (\mathbf{x}, \mathbf{w})$, and $p(\mathbf{z}|\mathcal{S}, \mathcal{D}) = p(\mathbf{x}|\mathcal{S})p(\mathbf{w}|\mathcal{D})$. This equation
 674 clearly shows that \mathbf{w} and \mathbf{x} are symmetric. Therefore, we obtain the formulas including both model
 675 and data uncertainty by replacing \mathbf{w} with joint random variable of \mathbf{x} and \mathbf{w} , i.e. $\mathbf{w} \rightarrow \mathbf{z} = (\mathbf{w}, \mathbf{x})$.

676 **Experiment.** Above, we claim two statements. First, the higher the dropout rate, the sharper the
 677 loss landscape. Second, the variance of the loss is inversely proportional to the ensemble size.

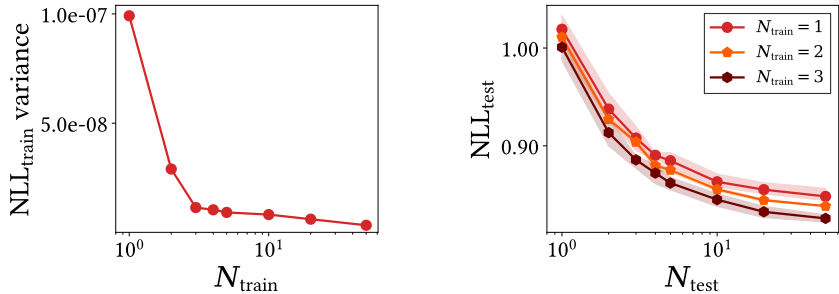
678 To demonstrate the former claim quantitatively, we compare the Hessian eigenvalue spectra and the
 679 Hessian max eigenvalue spectra of MC dropout with various dropout rates. In these experiments,
 680 we use ensemble size of one for MC dropout. For detailed explanation of Hessian max eigenvalue
 681 spectrum, see Appendix C.1.

682 Fig. D.3 represents the spectra, which reveals that *as the randomness of the model increases, the*
 683 *number of Hessian eigenvalue outliers increases.* Since outliers are detrimental to the optimization
 684 process (Ghorbani et al., 2019), dropout disturb NN optimization.

685 To show the latter claim, we evaluate the variance of NLL loss for ensemble size N_{train} as shown in
 686 Fig. D.4a. As we would expect, *the variance of the NLL loss—the sharpness of the loss landscape—is*
 687 *inversely proportional to the ensemble size for large N_{train} .*

688 D.4 TRAINING PHASE ENSEMBLE LEADS TO BETTER PERFORMANCE

689 Appendix D.3 raises an immediate question: *Is there a performance difference between ‘training*
 690 *with prediction ensemble’ and ‘training with a low MC dropout rate, instead of no ensemble’?* Note



(a) $\mathbb{V}[\mathcal{L}]$ for ensemble size on training dataset (b) NLL for ensemble size on test dataset

Figure D.4: **Training phase ensemble helps NN learn strong representation.** *Left:* The variance of NLL ($\mathbb{V}[\mathcal{L}]$) on training dataset is inversely proportional to the ensemble size for large N_{train} . See Eq. (24). *Right:* Training phase ensemble improves the predictive performance on test dataset.

691 that both methods reduce the sharpness of the loss landscape. This section answers the question
 692 by providing theoretical and experimental explanations that the ensemble in the training phase can
 693 improve predictive performance.

According to Gal & Ghahramani (2016), the total predictive variance (in regression tasks) is:

$$\sigma_{\text{pred}}^2 = \sigma_{\text{model}}^2 + \sigma_{\text{sample}}^2 \quad (28)$$

where σ_{model}^2 is model precision and σ_{sample}^2 is NN prediction variance. Therefore, the model precision is the lower bound of the predictive variance, i.e.:

$$\sigma_{\text{pred}}^2 \geq \sigma_{\text{model}}^2 \quad (29)$$

The model precision depends only on the model architecture. For example, in the case of MC dropout, σ_{model}^2 is proportional to the dropout rate (Gal & Ghahramani, 2016) as follows:

$$\sigma_{\text{model}}^2 \propto \text{dropout rate} \quad (30)$$

694 These suggest that model precision dominate predictive variance if the MC dropout rate is large
 695 enough, i.e., even if the number of ensembles is increased in the training phase, the predictive variance
 696 is almost the same. In contrast, decreasing the MC dropout rate reduces prediction diversity, and it
 697 obviously leads to performance degradation. Therefore, in the training phase, *it is better to ensemble*
 698 *predictions than to lower the MC dropout rate.* We believe that the training phase ensemble is strongly
 699 correlated with Batch Augmentation (Hoffer et al., 2020). We leave concrete analysis for future work.

700 **Experiment.** The experiments below support the theoretical analysis. We train MC dropout by
 701 using training-phase ensemble method with various ensemble sizes N_{train} .

702 As we would expect, Fig. D.4b shows that *training phase ensemble significantly improves the*
 703 *predictive performance.* In this experiment, we use MC dropout rate of 30%. As shown in Fig. A.1, it
 704 provides the best predictive performance. We use ensemble size $N_{\text{test}} = 50$ in test phase.

705 We also measure the predictive variances of NLL. The predictive variances of the model with
 706 $N_{\text{train}} = 1$ and with $N_{\text{train}} = 3$ are $\mathbb{V}[\mathcal{L}] = 0.0169$ and $\mathbb{V}[\mathcal{L}] = 0.0179$, respectively. Since the
 707 predictive variances of the two models are almost the same, we infer that there exists a lower bound.

708 E EXTENDED INFORMATIONS OF EXPERIMENTS

709 This section provides additional information on the experiments in Section 3.

710 E.1 IMAGE CLASSIFICATION

711 We present numerical comparisons in the image classification experiment and discuss the results in
 712 detail.

Table E.1: **Spatial smoothing improves both accuracy and uncertainty at the same time.** Predictive performance of models with spatial smoothing in image classification on CIFAR-10, CIFAR-100, and ImageNet.

MODEL & DATASET	MC DROPOUT	SMOOTH	NLL	Acc (%)	ECE (%)
VGG-19 & CIFAR-10	.	.	0.401 (-0.000)	93.1 (+0.0)	3.80 (-0.00)
	.	✓	0.376 (-0.002)	93.2 (+0.1)	5.49 (+1.69)
	✓	.	0.238 (-0.000)	92.6 (+0.0)	3.55 (-0.00)
	✓	✓	0.197 (-0.041)	93.3 (+0.7)	0.68 (-2.86)
ResNet-18 & CIFAR-10	.	.	0.182 (-0.000)	95.2 (+0.0)	2.75 (-0.00)
	.	✓	0.173 (-0.009)	95.4 (+0.2)	2.31 (-0.44)
	✓	.	0.157 (-0.000)	95.2 (+0.0)	1.14 (-0.00)
	✓	✓	0.144 (-0.014)	95.5 (+0.2)	1.04 (-0.10)
VGG-16 & CIFAR-100	.	.	2.047 (-0.000)	71.6 (+0.0)	19.2 (-0.0)
	.	✓	1.878 (-0.169)	72.2 (+0.6)	20.5 (+1.3)
	✓	.	1.133 (-0.000)	68.8 (+0.0)	3.66 (-0.00)
	✓	✓	1.034 (-0.099)	71.4 (+2.6)	1.06 (-2.60)
VGG-19 & CIFAR-100	.	.	2.016 (-0.000)	67.6 (+0.0)	21.2 (-0.0)
	.	✓	1.851 (-0.165)	71.7 (+4.0)	20.2 (-1.0)
	✓	.	1.215 (-0.000)	67.3 (+0.0)	6.37 (-0.00)
	✓	✓	1.071 (-0.144)	70.4 (+3.0)	2.15 (-4.22)
ResNet-18 & CIFAR-100	.	.	0.886 (-0.000)	77.9 (+0.0)	4.97 (-0.00)
	.	✓	0.863 (-0.023)	78.9 (+1.0)	4.40 (-0.57)
	✓	.	0.848 (-0.000)	77.3 (+0.0)	3.01 (-0.00)
	✓	✓	0.801 (-0.047)	78.9 (+1.6)	2.56 (-0.45)
ResNet-50 & CIFAR-100	.	.	0.835 (-0.000)	79.9 (+0.0)	8.88 (-0.00)
	.	✓	0.834 (-0.002)	80.7 (+0.8)	9.29 (+0.42)
	✓	.	0.822 (-0.000)	79.1 (+0.0)	6.63 (-0.00)
	✓	✓	0.800 (-0.022)	80.1 (+1.0)	7.25 (+0.62)
ResNeXt-50 & CIFAR-100	.	.	0.804 (-0.000)	80.6 (+0.0)	8.23 (-0.00)
	.	✓	0.825 (+0.022)	80.8 (+0.3)	9.41 (+1.18)
	✓	.	0.762 (-0.000)	80.5 (+0.0)	5.67 (-0.00)
	✓	✓	0.759 (-0.002)	80.7 (+0.2)	6.62 (+0.94)
ResNet-18 & ImageNet	.	.	1.210 (-0.000)	70.3 (+0.0)	1.62 (-0.00)
	.	✓	1.183 (-0.027)	70.6 (+0.3)	1.22 (-0.40)
	✓	.	1.215 (-0.000)	70.0 (+0.0)	1.39 (-0.00)
	✓	✓	1.190 (-0.032)	70.6 (+0.6)	2.25 (+0.86)
ResNet-50 & ImageNet	.	.	0.949 (-0.000)	76.0 (+0.0)	2.97 (-0.00)
	.	✓	0.916 (-0.033)	76.9 (+0.9)	3.46 (+0.49)
	✓	.	0.945 (-0.000)	76.0 (+0.0)	1.89 (-0.00)
	✓	✓	0.905 (-0.040)	77.0 (+1.0)	2.49 (+0.60)
ResNeXt-50 & ImageNet	.	.	0.919 (-0.000)	77.7 (+0.0)	3.63 (-0.00)
	.	✓	0.907 (-0.012)	78.0 (+0.3)	4.60 (+0.97)
	✓	.	0.895 (-0.000)	77.7 (+0.0)	2.53 (-0.00)
	✓	✓	0.887 (-0.008)	78.1 (+0.4)	3.28 (+0.75)

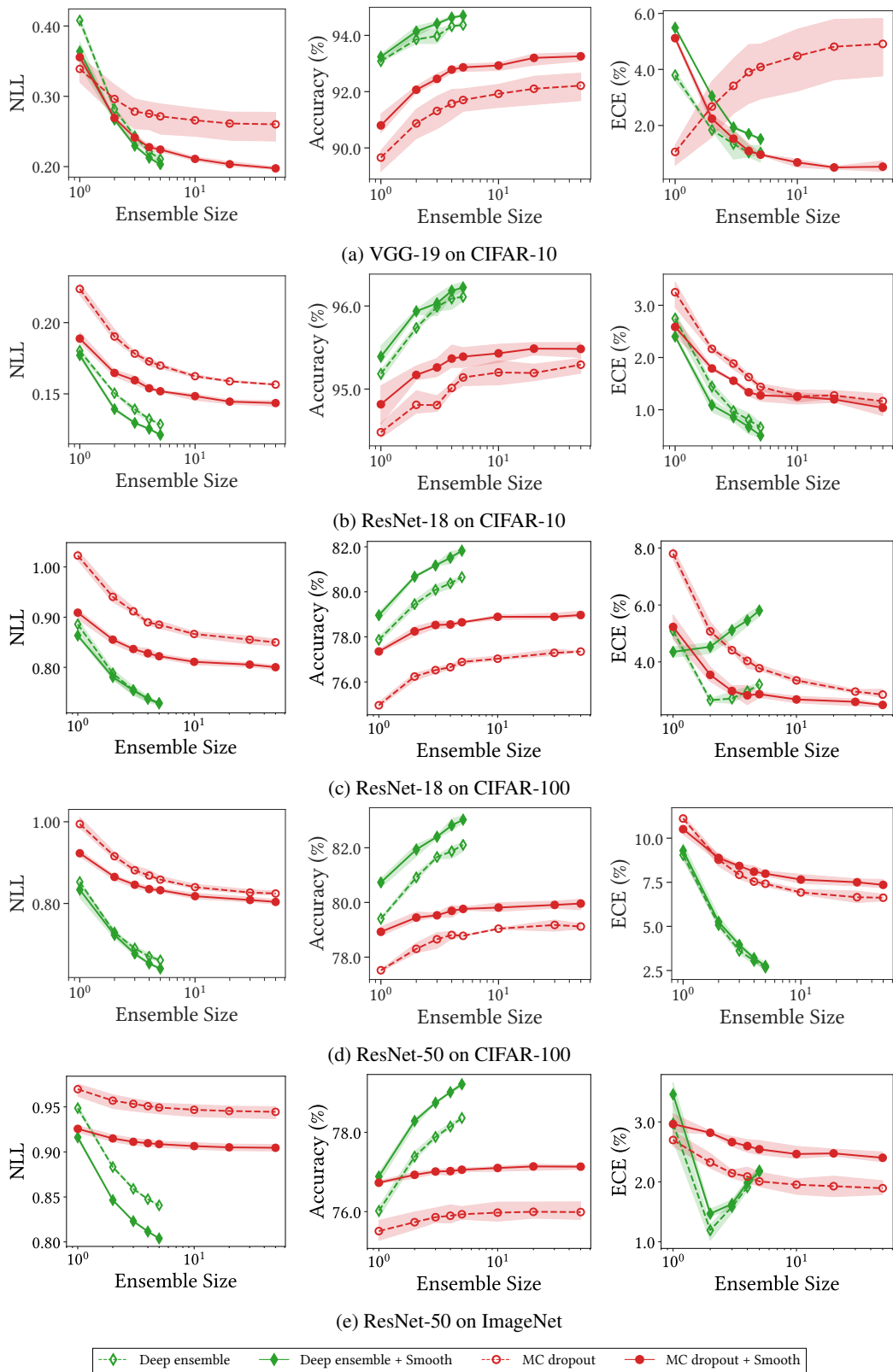


Figure E.1: **Spatial smoothing improves both accuracy and uncertainty across a whole range of ensemble sizes.**

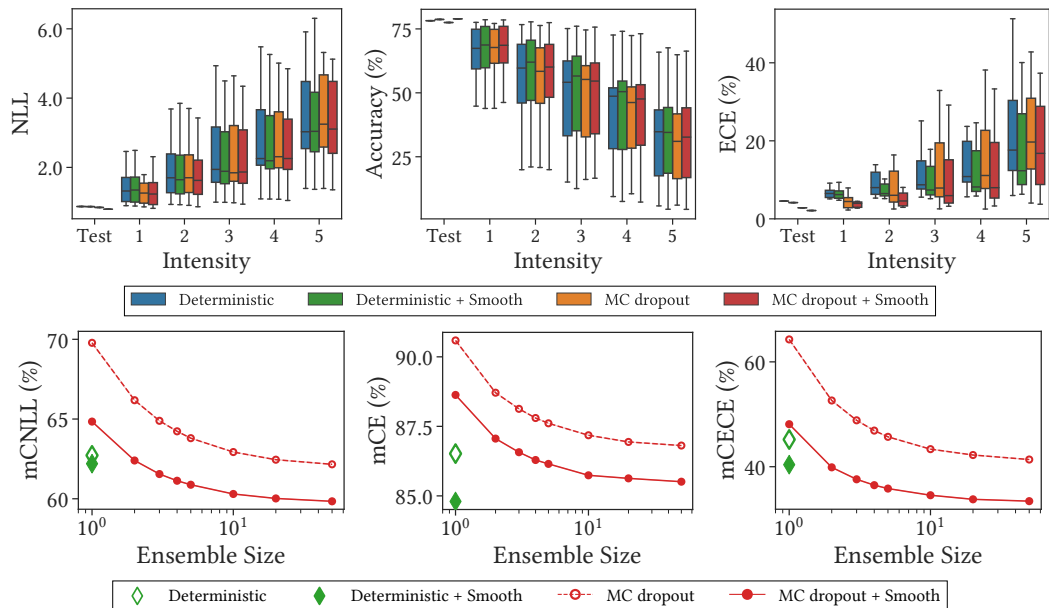


Figure E.3: **Spatial smoothing improves corruption robustness.** We measure the predictive performance of ResNet-18 on CIFAR-100-C. In the top row, we use an ensemble size of fifty for MC dropout with and without spatial smoothing.

713 **Computational performance.** The throughput of MC dropout and “MC dropout + spatial smoothing” is 755 and 675 image/sec, respectively, in training phase on ImageNet. As mentioned in lines
 714 Section 3.1, NLL of “MC dropout + spatial smoothing” with ensemble size of 2 is comparable
 715 to or even better than that of MC dropout with ensemble size of 50. Therefore, “MC dropout +
 716 spatial smoothing” is $22\times$ faster than MC dropout with similar predictive performance, in terms of
 717 throughput.
 718

719 **Predictive performance on test dataset.** Fig. E.2 represents the reliability diagram of ResNet-18 on CIFAR-100,
 720 which shows that spatial smoothing improves the uncertainty of both deterministic and Bayesian NNs. Numerical compar-
 721 isons are provided below.
 722
 723

724 Table E.1 shows the predictive performance of various deterministic and Bayesian NNs with and without spatial smoothing
 725 on CIFAR-10, CIFAR-100, and ImageNet. This table
 726 suggests the following: First, spatial smoothing improves
 727 both accuracy and uncertainty in most cases. In particular, *it*
 728 *improves the predictive performance of all models with MC*
 729 *dropouts.* Second, spatial smoothing significantly improves
 730 the predictive performance of VGG compared with ResNet.
 731 VGG has a chaotic loss landscape, which results in poor predictive
 732 performance (Li et al., 2018), and spatial smoothing
 733 smoothens its loss landscape effectively. Third, as the depth
 734 increases, the performance improvement decreases. Deeper
 735 NNs provide more overconfident results (Guo et al., 2017),
 736 but the number of spatial smoothing layers calibrating uncer-
 737 tainty is fixed. Last, the performance improvement of ResNeXt, which includes an ensemble in its
 738 internal structure, is relatively marginal.
 739

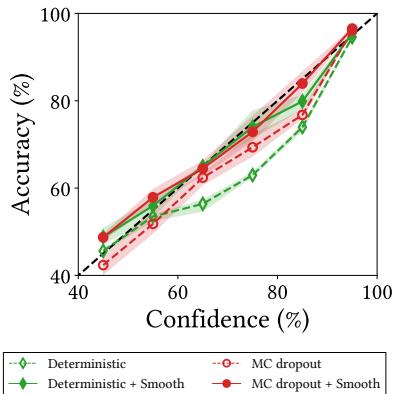


Figure E.2: **Spatial smoothing calibrates predictions.** We present reliability diagram of ResNet-18 on CIFAR-100.

740 Fig. E.1 shows predictive performance of MC dropout and deep ensemble for ensemble size. A
 741 deep ensemble with an ensemble size of 1 is a deterministic NN. This figure shows that spatial
 742 smoothing improves efficiency of ensemble size and the predictive performance at ensemble size of

Table E.2: **Spatial smoothing improves adversarial robustness.** We measure the accuracy (ACC) and the Attack Success Rate (ASR) of ResNet-50 against adversarial attacks on ImageNet.

ATTACK	MC DROPOUT	SMOOTH	ACC (%)	ASR (%)
FGSM	·	·	28.3 (+0.0)	62.9 (-0.0)
	·	✓	30.3 (+2.0)	60.5 (-2.4)
	✓	·	30.3 (+0.0)	59.8 (-0.0)
	✓	✓	32.6 (+2.3)	57.4 (-2.4)
PGD	·	·	7.5 (+0.0)	90.1 (-0.0)
	·	✓	9.0 (+1.4)	88.2 (-1.9)
	✓	·	12.2 (+0.0)	83.7 (-0.0)
	✓	✓	13.7 (+1.5)	82.1 (-1.6)

743 50. In addition, spatial smoothing stabilizes NN training. It reduces the variance of the performance,
744 especially in VGG.

745 A peculiarity of the results on ImageNet is that spatial smoothing degrades ECE of ResNet-50. It
746 is because spatial smoothing significantly improves the accuracy in this case, and there tends to be
747 a trade-off between accuracy and ECE, e.g. as shown in (Guo et al., 2017), Fig. A.1, and Fig. B.3.
748 Instead, spatial smoothing shows the improvement in NLL, another uncertainty metric.

749 **Predictive performance on training datasets.** Note that *spatial smoothing helps NN learn strong*
750 *representations*. In other words, *spatial smoothing does not regularize NNs*. For example, NLL
751 ResNet-18 with MC dropout on CIFAR-100 training dataset is 2.20×10^{-2} . The NLL of the ResNet
752 with spatial smoothing is 1.94×10^{-2} . In conclusion, spatial smoothing reduces the training loss.

753 **Corruption robustness.** We measure predictive performance on CIFAR-100-C (Hendrycks &
754 Dietterich, 2019) in order to evaluate the robustness of the models against 5 intensities and 15 types
755 of data corruption. The top row of Fig. E.3 shows the results as a box plot. The box plot shows the
756 median, interquartile range (IQR), minimum, and maximum of predictive performance for types.
757 They reveal that spatial smoothing improves predictive performance for corrupted data. In particular,
758 spatial smoothing undoubtedly helps in predicting reliable uncertainty.

To summarize the performance of corrupted data in a single value, Hendrycks & Dietterich (2019)
introduced a corruption error (CE) for quantitative comparison. CE_c^f , which is CE for corruption type
 c and model f , is as follows:

$$CE_c^f = \left(\sum_{i=1}^5 E_{i,c}^f \right) / \left(\sum_{i=1}^5 E_{i,c}^{\text{AlexNet}} \right) \quad (31)$$

where $E_{i,c}^f$ is top-1 error of f for corruption type c and intensity i , and $E_{i,c}^{\text{AlexNet}}$ is the error of AlexNet.
Mean CE or mCE summarizes CE_c^f by averaging them over 15 corruption types such as Gaussian
noise, brightness, and show. Likewise, to evaluate robustness in terms of uncertainty, we introduce
corruption NLL ($CNLL$, \downarrow) and corruption ECE ($CECE$, \downarrow) as follows:

$$CNLL_c^f = \left(\sum_{i=1}^5 NLL_{i,c}^f \right) / \left(\sum_{i=1}^5 NLL_{i,c}^{\text{AlexNet}} \right) \quad (32)$$

and

$$CECE_c^f = \left(\sum_{i=1}^5 ECE_{i,c}^f \right) / \left(\sum_{i=1}^5 ECE_{i,c}^{\text{AlexNet}} \right) \quad (33)$$

Table E.3: **Spatial smoothing improves the consistency, robustness against shift-perturbation.** We measure the consistency of ResNet-18 on CIFAR-10-P. Deterministic NN with $N = 5$ means deep ensemble.

MC DROPOUT	SMOOTH	N	CONS (%)	CEC ($\times 10^{-2}$)
.	.	1	97.9 (+0.0)	1.03 (-0.00)
.	✓	1	98.2 (+0.3)	1.16 (+0.13)
.	.	5	98.7 (+0.0)	1.22 (-0.00)
.	✓	5	98.9 (+0.2)	1.33 (+0.11)
✓	.	50	98.2 (+0.0)	1.29 (-0.00)
✓	✓	50	98.4 (+0.2)	1.34 (+0.05)

759 where $NLL_{i,c}^f$ and $ECE_{i,c}^f$ are NLL and ECE of f for c and i , respectively. $mCNLL$ and $mCECE$
 760 are averages over corruption types. Experimental results show that spatial smoothing improves the
 761 robustness against data corruption. See Fig. E.3 for the results.

762 The bottom row of Fig. E.3 shows mCNLL, mCE, and mCECE for ensemble size. They indicates that
 763 spatial smoothing improves not only the efficiency but corruption robustness across a whole range of
 764 ensemble size.

765 **Adversarial robustness.** We show that spatial smoothing also improves adversarial robustness.
 766 First, we measure the robustness, in terms of accuracy and attack success rate (ASR), of ResNet-
 767 50 on ImageNet against popular adversarial attacks, namely FGSM (Goodfellow et al., 2015) and
 768 PGD (Madry et al., 2018). Table E.2 indicate that both MC dropout and spatial smoothing improve
 769 robustness against adversarial attacks.

770 Next, we find out how spatial smoothing improves adversarial robustness. To this end, similar
 771 to Section 2.2, we measure the accuracy on the test datasets with frequency-based adversarial
 772 perturbations. In this experiment, we use FGSM attack. This experimental result shows that spatial
 773 smoothing is particularly robust against high frequency ($\geq 0.3\pi$) adversarial attacks. This is because
 774 spatial smoothing is a low-pass filter, as we mentioned in Section 2.2. Since the ResNet is vulnerable

775 against high frequency adversarial attack, an effective defense of spatial smoothing against high
 776 frequency attacks significantly improves the robustness.
 777
 778

Consistency. To evaluate the translation invariance of models, we use *consistency* (Hendrycks & Dietterich, 2019; Zhang, 2019a), a metric representing translation consistency for shift-translated data sequences $\mathcal{S} = \{\mathbf{x}_1, \dots, \mathbf{x}_{M+1}\}$, as follows:

$$\text{Consistency} = \frac{1}{M} \sum_{i=1}^M \mathbb{1}(g(\mathbf{x}_i) = g(\mathbf{x}_{i+1})) \quad (34)$$

779 where $g(\mathbf{x}) = \arg \max p(\mathbf{y}|\mathbf{x}, \mathcal{D})$. Table E.3 provides consistency of ResNet-18 on CIFAR-10-P
 780 (Hendrycks & Dietterich, 2019). The results shows that MC dropout and deep ensemble improve consistency,
 781 and spatial smoothing improves consistency of both deterministic and Bayesian NNs.
 782
 783
 784

Prior works (Zhang, 2019a; Azulay & Weiss, 2019) investigated the fluctuation of predictive confidence

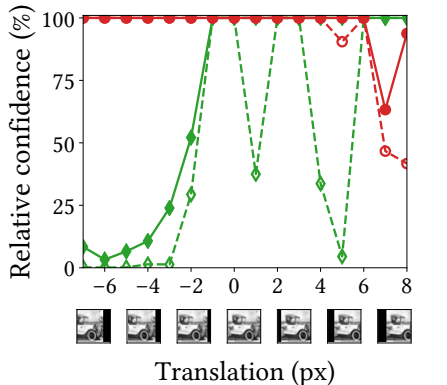


Figure E.4: **Spatial smoothing improves the confidence when the predictions are incorrect.** We define relative confidence (See Eq. (36)), and measure the metric of ResNet-18 on CIFAR-10-P.

Table E.4: **Spatial smoothing and temporal smoothing are complementary.** We provide predictive performance of MC dropout in semantic segmentation on CamVid for each method. SPAT and TEMP each stand for spatial smoothing and temporal smoothing. CONS stands for consistency.

MC DROPOUT	SPAT	TEMP	N	NLL	ACC (%)	ECE (%)	CONS (%)
.	.	.	1	0.354 (+0.000)	92.3 (+0.0)	4.95 (+0.00)	95.1 (+0.0)
.	✓	.	1	0.318 (+0.036)	92.4 (+0.1)	4.54 (+0.41)	95.5 (+0.4)
.	.	✓	1	0.290 (+0.064)	92.5 (+0.2)	3.18 (+1.77)	96.3 (+1.2)
.	✓	✓	1	0.278 (+0.076)	92.5 (+0.2)	3.03 (+1.92)	96.6 (+1.5)
✓	.	.	50	0.298 (+0.000)	92.5 (+0.0)	4.20 (+0.00)	95.4 (+0.0)
✓	✓	.	50	0.284 (+0.014)	92.6 (+0.1)	3.96 (+0.24)	95.6 (+0.2)
✓	.	✓	1	0.273 (+0.025)	92.6 (+0.1)	3.23 (+0.97)	96.4 (+1.0)
✓	✓	✓	1	0.260 (+0.038)	92.6 (+0.1)	2.71 (+1.49)	96.5 (+1.1)

on shift-translated data sequence. However, surprisingly, we find that *confidence fluctuation has little to do with consistency*. To demonstrate this claim, we introduce cross-entropy consistency (CEC, ↓), a metric that represents the fluctuation of confidence on a shift-translated data sequence $\mathcal{S} = \{\mathbf{x}_1, \dots, \mathbf{x}_{M+1}\}$, as follows:

$$\text{CEC} = -\frac{1}{M} \sum_{i=1}^M f(\mathbf{x}_i) \cdot \log(f(\mathbf{x}_{i+1})) \quad (35)$$

785 where $f(\mathbf{x}) = p(\mathbf{y}|\mathbf{x}, \mathcal{D})$. In Table E.3, high consistency does not mean low CEC; conversely, high
 786 consistency tends to be high CEC. Canonical NNs predict overconfident probabilities, and their
 787 confidence sometimes changes drastically from near-zero to near-one. Correspondingly, it results in
 788 low consistency but low CEC. On the contrary, well-calibrated NNs such as MC dropout provide
 789 confidence that oscillates between zero and one, which results in high CEC.

To represent the NN reliability properly, we propose *relative confidence* (↑) as follows:

$$\text{Relative confidence} = p(y_{\text{true}}|\mathbf{x}, \mathcal{D}) / \max p(\mathbf{y}|\mathbf{x}, \mathcal{D}) \quad (36)$$

790 where $\max p(\mathbf{y}|\mathbf{x}, \mathcal{D})$ is confidence of predictive result and $p(y_{\text{true}}|\mathbf{x}, \mathcal{D})$ is probability of the result
 791 for true label. It is 1 when NN classifies the image correctly, and less than 1 when NN classifies it
 792 incorrectly. Therefore, relative confidence is a metric that indicates the overconfidence of a prediction
 793 when NN’s prediction is incorrect.

794 Figure E.4 shows a qualitative example of consistency on CIFAR-10-P by using relative confidence.
 795 This figure suggests that spatial smoothing improves consistency of both deterministic and Bayesian
 796 NN.

797 E.2 SEMANTIC SEGMENTATION

798 Table E.4 shows the performance of U-Net on the CamVid dataset. This table indicates that spatial
 799 smoothing improves accuracy, uncertainty, and consistency of deterministic and Bayesian NNs.
 800 This is consistent with the results in image classification. In addition, temporal smoothing leads
 801 to significant improvement in efficiency of ensemble size, accuracy, uncertainty, and consistency
 802 by exploiting temporal information. Moreover, temporal smoothing requires only one ensemble
 803 to achieve high predictive performance, since it cooperates with the temporally previous predictions. *We*
 804 *obtain the best predictive and computational performance by using both temporal smoothing and*
 805 *spatial smoothing.*

806 F COMPARISON WITH ANTI-ALIASED CNN

807 As we mentioned in [Section 4](#), local means (Blur), also known as anti-aliased CNN ([Zhang, 2019a](#)),
808 improve accuracy. Nevertheless, our work (Prob + Blur) has novelties in three respects: different
809 motivation, improved uncertainty estimation, and analysis of how spatial smoothing works.

810 **Different motivation.** The motivation of local means was to mitigate the aliasing effect of subsam-
811 pling and to improve shift invariance. In contrast, our spatial smoothing is introduced to aggregate
812 and ensemble nearby feature map points.

813 **Improved uncertainty estimation.** We demonstrate that spatial smoothing improves not only
814 accuracy, but also uncertainty estimation and robustness against natural corruptions and adversarial
815 attacks all at the same time. Moreover, we show that spatial smoothing significantly enhances the
816 performance of MC dropout. Since there typically tends to be a trade-off between accuracy and
817 “uncertainty + robustness”—e.g. as shown in ([Guo et al., 2017](#); [Zhang et al., 2019](#); [Geirhos et al.,](#)
818 [2019](#); [Zhang, 2019b](#)), [Fig. A.1](#), and [Fig. B.3](#)—in NN modeling, we believe our simple yet effective
819 method makes major inroads into the uncertainty quantification and generalization.

820 **Analysis of how spatial smoothing improves performance.** We find that the predictive perfor-
821 mance improvement is *not* due to the anti-aliasing effect of local means.

- 822 • Prob + Blur—our probabilistic spatial smoothing—improves the performance of pre-
823 activation CNNs, but Blur alone—local mean or anti-aliased CNN—does not. In fact,
824 contrary to ([Zhang, 2019a](#)), local mean degrades the predictive performance since it results
825 in loss of information. It suggests that Prob plays an key role in prediction. For more details,
826 see [Appendix F.1](#).
- 827 • Although the local filtering can result in loss of information, [Zhang \(2019a\)](#) experimentally
828 observed an increase in both shift-invariance (as expected) and accuracy (which was be-
829 yond expectation). However, “there exist a fundamental trade-off between ‘shift-invariance
830 plus anti-aliasing’ and performance” ([Zhang, 2019b](#)). Moreover, it is difficult to relate
831 anti-aliasing to improved uncertainty and robustness. [Zhang \(2019a\)](#) did not provide an
832 explanation for these phenomena. As discussed in [Appendix E.1](#), spatial smoothing helps
833 NNs learn strong representations, not regularizes NNs.
- 834 • Spatial smoothing is, surprisingly, robust against blur corruptions.

835 We analyze how spatial smoothing improves predictive performance, by using loss landscape vi-
836 sualization, Hessian eigenvalue spectra, and Fourier analysis. These analyzes draw the following
837 conclusions:

- 838 • *Loss landscape visualization:* Spatial smoothing stabilizes loss landscape fluctu-
839 ations, caused by e.g. MC dropout. This results in stabilizing NN training
840 and improving performance as well as generalization. See [Figs. 8](#) and [C.2](#).
841 See also `code/resources/losslandscapes/resnet_mcdo_18.gif` and
842 `code/resources/losslandscapes/resnet_mcdo_smoothing_18.gif` in the
843 supplementary material.
- 844 • *Hessian eigenvalue spectra:* Spatial smoothing suppresses outliers of Hessian eigenvalues,
845 which disrupt NN training. See [Figs. 7](#) and [C.3](#).
- 846 • *Fourier analysis:* Spatial smoothing effectively removes high frequency signals, including
847 noise due to MC dropout. We also show that CNNs are vulnerable to high frequency noise
848 and high frequency adversarial attacks. See [Figs. 6](#) and [D.2](#).

849 We also provide theoretical analysis of how spatial smoothing works. We prove that *dropout sharpens*
850 *the loss landscape, and ensemble smoothens it*. Since the spatial smoothing is a spatial ensemble, it
851 significantly enhances the performance of MC dropout. See [Appendix D.3](#) for more details. Further-
852 more, we also show that *training-phase ensemble significantly improves the predictive performance*
853 *because it smoothens the loss landscape without loss of prediction diversity*. Therefore, the spatial
854 smoothing, which ensembles feature map points at training time, improves the performance effectively.
855 See [Appendix D.4](#).

856 F.1 PROB PLAYS AN IMPORTANT ROLE IN SPATIAL SMOOTHING

857 As discussed in Section 2.1, we take the perspective that each point in feature map is a prediction for
 858 binary classification by deriving the Bernoulli distributions from the feature map by using Prob. It is
 859 in contrast to previous works known as sampling-free BNNs (Hernández-Lobato & Adams, 2015;
 860 Wang et al., 2016; Wu et al., 2019) attempting to approximate the distribution of feature map with
 861 one Gaussian distribution. We do not use any assumptions on the distribution of feature map, and
 862 exactly represent the Bernoulli distributions and their averages. However, sampling-free BNNs are
 863 error-prone because there is no guarantee that feature maps will follow a Gaussian distribution.

This Prob plays an important role in spatial smoothing. CNNs such as VGG, ResNet, and ResNeXt generally use post-activation arrangement. In other words, their stages end with BatchNorm and ReLU. Therefore, spatial smoothing layers $\text{Smooth}(z) = \text{Blur} \circ \text{Prob}(z)$ in CNNs cooperates with BatchNorm and ReLU as follows:

$$\text{Prob}(z) = \text{ReLU} \circ \tanh_{\tau} \circ \text{ReLU} \circ \text{BatchNorm}(z) \tag{37}$$

$$= \text{ReLU} \circ \tanh_{\tau} \circ \text{BatchNorm}(z) \tag{38}$$

864 since ReLU and \tanh_{τ} are commutative, and $\text{ReLU} \circ \text{ReLU}$ is ReLU. This Prob is trainable and is a
 865 general form of Eq. (7). If we only use Blur as spatial smoothing, the activations BatchNorm-ReLU
 866 play the role of Prob.

867 In order to analyze the roles of Prob and Blur more precisely, we measure the predictive performance
 868 of the model that does not use the post-activation. Figure F.1 shows NLL of pre-activation
 869 VGG-16 on CIFAR-100. The result shows that Blur with Prob improves the performance, but
 870 Blur alone does not. In fact, contrary to (Zhang, 2019a), *blur degrades the predictive performance*
 871 *since it results in loss of information*. We also measure the performance of VGG-19, ResNet-18,
 872 ResNet-50, and BlurPool (Zhang, 2019a) with pre-activation, and observe the same phenomenon. In
 873 addition, BatchNorm-ReLU in front of GAP significantly improves the performance of pre-activation
 874 ResNet.

882 As mentioned in Appendix C.2, pre-activation is a special case of spatial smoothing. Therefore, the
 883 performance improvement of pre-activation by spatial smoothing is marginal compared to that of post-
 884 activation.

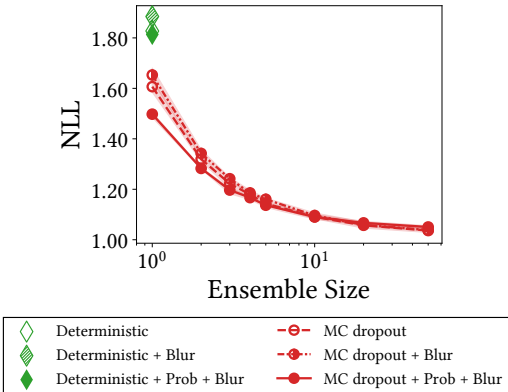


Figure F.1: **Blur alone harms the predictive performance, although Prob + Blur improves it.** We provide NLL of pre-activation VGG-16 on CIFAR-100.